

**Near Infrared Light in the Brain:
A Review of Current NIR Technology and its
Application to Studying Brain Function**

Jason Tokayer

August 21, 2008

Directed Research Report, Spring '08-Summer '08

Under the Guidance of Dr. B. Keith Jenkins

USC, Department of Electrical Engineering-Systems

Table of Contents

CHAPTER 1: INTRODUCTION	3
CHAPTER 2: STRUCTURE OF THE BRAIN	5
CHAPTER 3: SIGNALS IN THE BRAIN	9
3.1: Electrical Signals	9
3.1.1: EEG-Based Signals	9
3.1.2: ECoG	10
3.1.3: MRI	11
3.2: Optical Signals	11
3.2.1: Slow Signal	11
3.2.2: Fast Signal	19
CHAPTER 4: BRAIN SIGNAL PROCESSING	24
4.1: Introduction	24
4.2: General Techniques	25
4.2.1: Independent Component Analysis (ICA)	25
4.2.2: Common Spatial Patterns (CSP)	26
4.2.3: Common Sparse Spectral Spatial Pattern (CSSSP)	28
4.2.4: Dynamic Factor Analysis	29
4.2.5: Wiener Filtering	30
4.2.6: AR Estimation	30
4.2.7: Consistency Measures	30
4.3: Processing Techniques for Optical Data	33
4.4: Software Packages for Optical Data Processing	36
CHAPTER 5: Path of Light in the Brain	38
5.1: Introduction	38
5.2: Tissue Optical Properties via Experiment	39
5.3: Transport Theory	43
5.3.1: Radiative Transfer Equation (From [62])	43
5.3.2: Diffusion Approximation	44
5.3.3: Photon Density	45
5.4: Simulation Methods	47
5.4.1: Monte Carlo Methods	47
5.4.2: Finite Element Methods	51
6.1: Sources and Detectors	54
6.2: Optode Placement	55
6.3: Encoding Schemes	57
6.4: Spectroscopy Systems	59
6.4.1: Continuous Wave	59
6.4.2: Time-Resolved	59
6.4.3: Frequency Domain	60
6.4.4: Comparison	63
6.5: Examples	64
CHAPTER 7: FAST SIGNAL EXPERIMENTAL RESULTS	65
CHAPTER 8: OTHER OPTICAL METHODS	66
8.1: Optical Coherence Tomography	66

8.2: Imaging with Voltage-Sensitive Dyes	66
8.3: Optical Probes	67
8.4: Optical Phase Conjugation	67
8.5: Other Methods	69
CHAPTER 9: BRAIN COMPUTER INTERFACES (BCIS)	70
9.1: Introduction	70
9.2: Performance	71
9.3: Optical BCIs	72
9.4: Other BCIs	74
CHAPTER 10: UNEXPLORED RESEARCH QUESTIONS	76
REFERENCES	78

CHAPTER 1: INTRODUCTION

There exists a window of wavelengths in the near infrared (NIR) range (650-900nm) in which photons can penetrate tissue deep enough so as to illuminate the outer part of the cerebral cortex¹. Water is one of the principle absorbers of light in the head. Outside of the NIR range, water absorbs most of the light that is shone into the head. On the other hand, the absorption coefficient of water is relatively low in the NIR region², thus allowing this light to leave the head before it is absorbed. Therefore, this region of the electromagnetic spectrum is termed the optical window for brain tissue interrogation.

NIR light can penetrate several centimeters into tissue. Because of the relatively large size of the human head and its scattering properties, NIR light diffuses quickly after being shone into the head. The diffusion parameters are influenced by physiological events in the brain and are related to changes in the absorption and scattering properties of brain tissue³. Absorption leads to radiation-less loss of energy or induces either fluorescence, in which absorption triggers emission of another with a longer wavelength, or phosphorescence, which is similar to but slower than fluorescence. Scattering can be observed at unchanged frequencies or accompanied by a Doppler shift due to moving particles⁴. These changes can be observed using NIR techniques instrumentation.

There are many ways to record brain signals without using light. One of the most common ways is to use electrical signals in the brain. Each of the methods has either good spatial resolution but poor temporal resolution or good temporal resolution but poor spatial resolution. An example of the former is functional magnetic resonance imaging, or fMRI, and an example of the latter is electroencephalography, or EEG. Unlike these techniques, optical methods are capable of having both good temporal and good spatial resolutions. Other advantages of optical methods and instrumentation include low-cost, safety, repeatability of experiments, portability⁵ and less sensitivity to some types of artifacts, such as eye movements, than electrical methods. Also, unlike EEG, optical methods are not

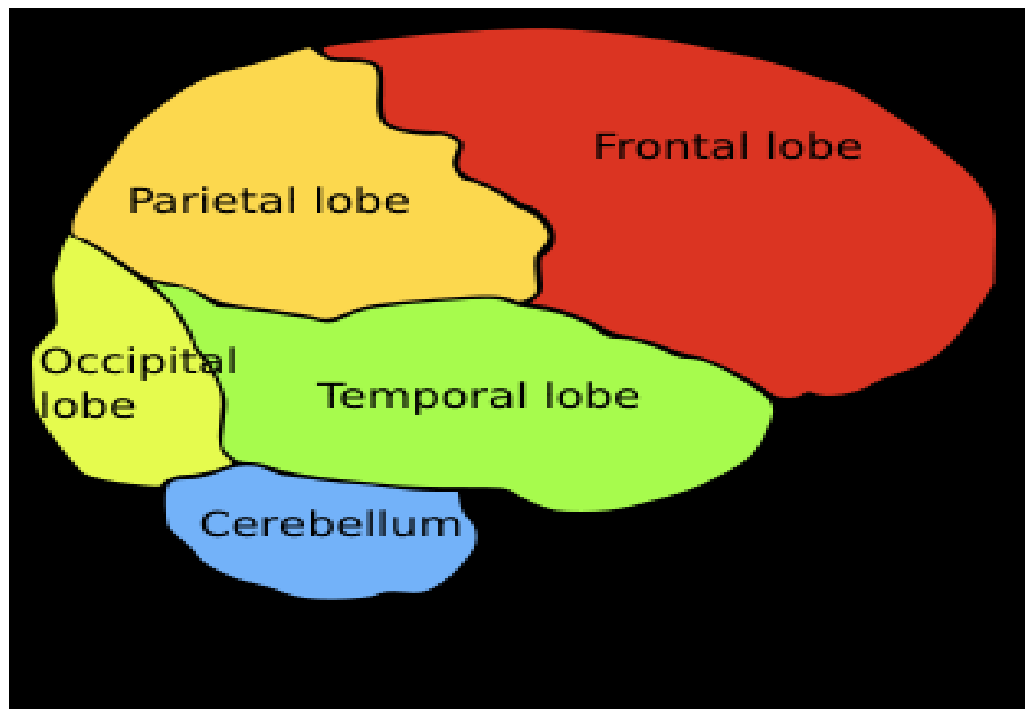
sensitive to geometrical configuration of the individual neurons. These advantages make optical methods particularly useful when studying both neural and vascular activity.

The current paper is a summary of the work I did during the spring 2008 semester. I begin with a look at the structure of the brain, and move to brain signals and related signal processing techniques. I then explain some optical instrumentation designs. The second to last chapter discusses brain computer interfaces, and the last chapter notes some research questions that have yet to be explored. All of this work was done under the guidance of Dr. B. Keith Jenkins, who met with me weekly to both discuss the papers that I read for the week and guide me in the right direction.

CHAPTER 2: STRUCTURE OF THE BRAIN

The brain can be viewed as a complex information processing machine, with sub-modules specialized for different types of psychological functions. This model of the brain, the distributed model, assumes that a number of different sub-processes interact to produce final overt behavior. Underlying the overt behavior are a number of physiological changes that can be observed using appropriate instrumentation. Physiological measures are believed to possess varying degrees of spatial, temporal and/or functional specificity. The validity of any experimental results depends on the validity of assumptions about the nature, configuration and specificity of the underlying structures in the brain. A combined spatio-temporal approach, that also assesses functional specificity, is thus particularly useful in the study of the interactions and correlations among the activities of different brain areas⁶.

Here are two views of the human cerebral cortex, one divided into the four lobes and the other a functional brain map.



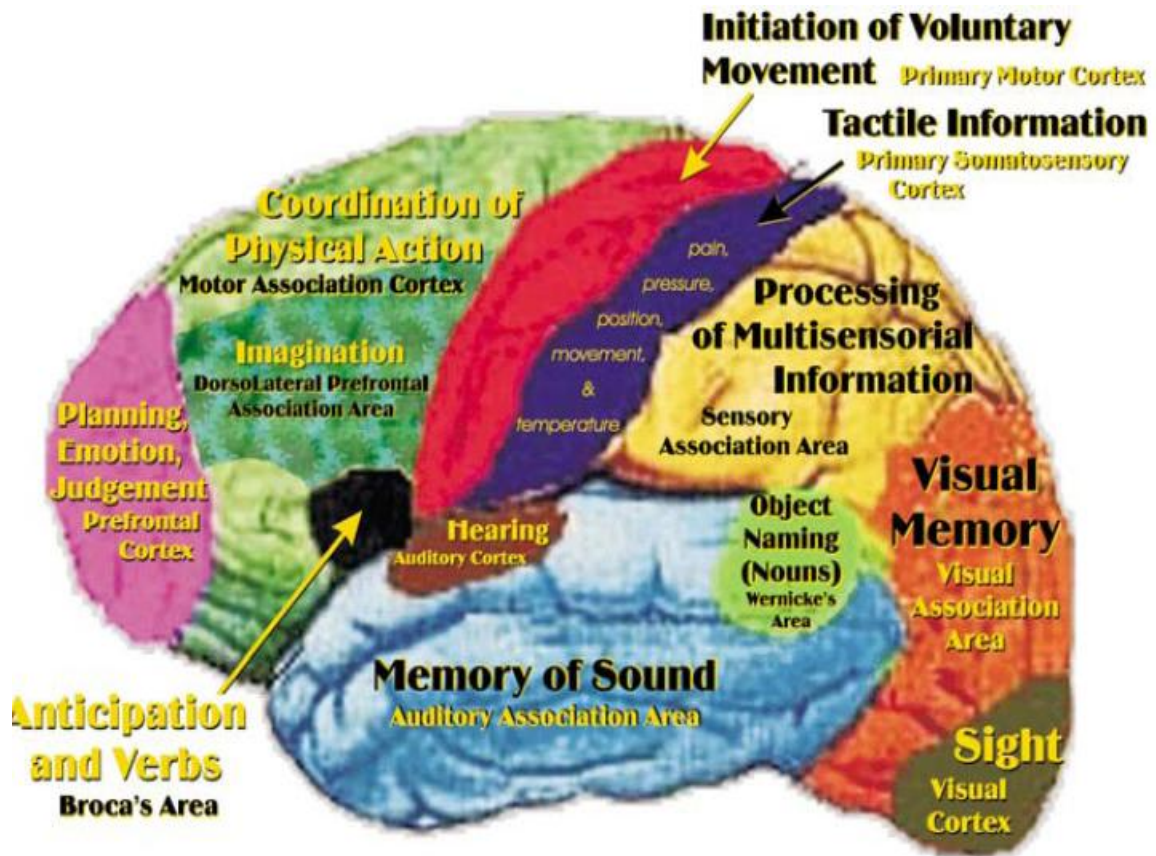


Figure 1: Regions of the Brain. Top from [7] and bottom from [8]

Each of the lobes provides specific functionality. In brief, the frontal lobe is associated with pleasure, long-term memory planning and drive. As the name implies, it is located on the front of the head. On the top panel above it is red, whereas on the bottom panel it is pink. The occipital lobe is located in the back of the head, and is the visual processing center of the mammalian brain, containing the visual cortex. The temporal lobe, located on the sides of the head, is involved in auditory processing and houses the primary auditory cortex. It is blue in the bottom panel above. The temporal lobe is also heavily involved in semantic both in speech and vision. It also contains the hippocampus and is therefore involved in memory formation as well. Finally, the parietal lobe takes care of sensory information and integrates it from different modalities. In particular, the parietal lobe is useful in determining spatial sense and

navigation. It is separated from the frontal lobe by the primary motor cortex, which controls voluntary movements of specific body parts⁹. On the bottom panel above the parietal lobe is shaded yellow. A clearer picture of the primary motor cortex is given below:

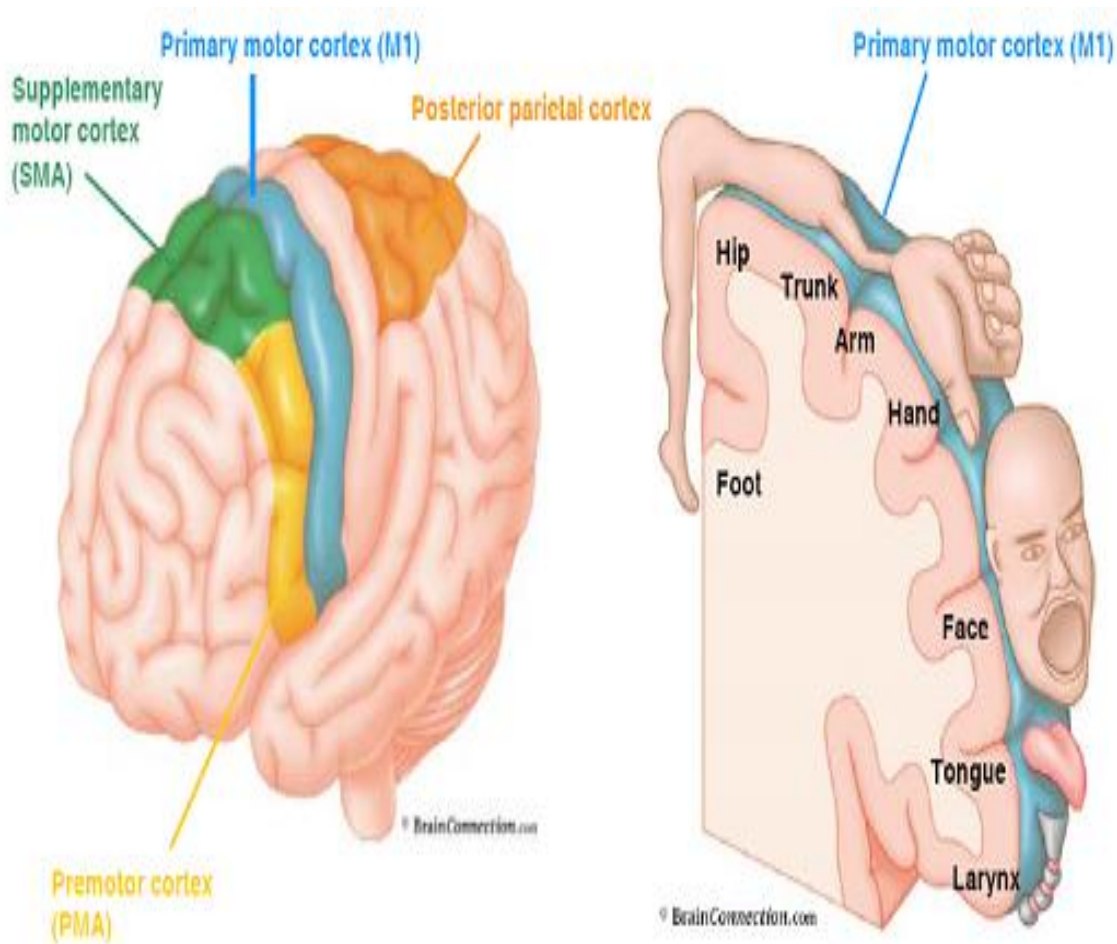


Figure 2: The Primary Motor Cortex. From [10]

In humans, the brain is surrounded by tissues that separate the skull from the brain. The surrounding tissues consist of the dura mater, arachnoid mater, and pia mater. Below the arachnoid is the subarachnoid space which contains cerebrospinal fluid, a substance that protects the nervous system. Blood vessels enter the central nervous system above the pia mater. The cells in the blood vessel walls are joined tightly, forming the blood-brain barrier which protects the brain from toxins that might enter through the blood³⁷.

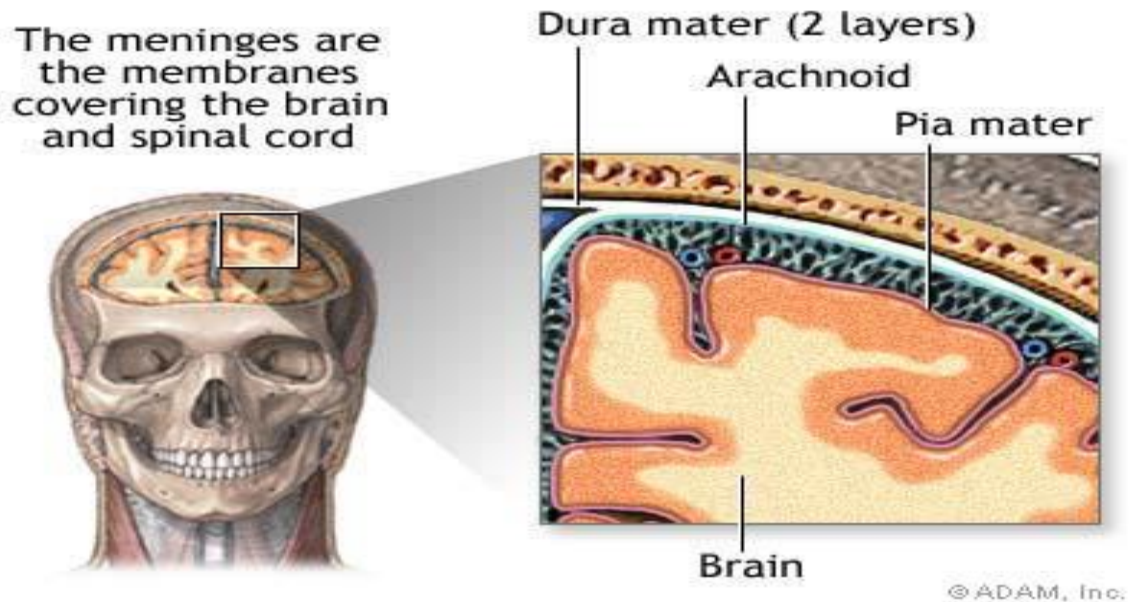


Figure 3: Layered Covering of the Brain. From

<http://www.nytimes.com/imagepages/2007/08/01/health/adam/19080Meningesofthebrain.html>

One final note on the structure of the brain relates to the types of matter in it. Gray matter is distributed at the surface of the cerebral cortex and of the cerebellum. This type of matter consists largely of cell bodies of the neurons. On the other hand, white matter forms the bulk of the deep parts of the brain and the superficial parts of the spinal chord. Unlike gray matter, white matter consists largely of bundles of axons¹¹. In this way, the white matter acts more like a routing unit while the gray matter acts more like a processing unit. It is important to note that most cognitive function can be examined from the shallow layers of the brain, and specifically the gray matter.

CHAPTER 3: SIGNALS IN THE BRAIN

3.1: Electrical Signals

A variety of electrical techniques are available for measuring signals in the brain. Electrophysiological techniques rely directly on neural activity while hemodynamic methods measure some slower physiological response and assume a correlation between it and underlying neural activity. Electrophysiological techniques, such as EEG, are most useful for determining where activity occurs, while hemodynamic methods, such as fMRI, are most useful for determining where brain activity occurs¹².

3.1.1: EEG-Based Signals

Scalp electroencephalography (EEG) measures the summed activity of post-synaptic currents. An action potential in a pre-synaptic axon causes the release of a neurotransmitter into the synapse that eventually binds to receptors in a post-synaptic dendrite, resulting in a flow of ions into or out of the dendrite, which in turn results in compensatory currents in the extracellular space. It is these extracellular currents that generate EEG voltages¹³. Note that EEG is most sensitive to activity of pyramidal neurons (output cells of cortex) and to postsynaptic activity measurable in the dendrites rather than in the axons¹⁴.

EEG uses multiple scalp electrodes to record a wide range of signals generated by synchronous changes in postsynaptic potentials emanating from thousands of neurons. These synchronies are divided into different frequency ranges within the .3 to 20+ Hz range¹⁵. There is the low frequency delta band, which lies between .3 and 3Hz, the theta band, from 4 to 7 Hz, the alpha band, from 8 to 12 Hz, the beta band, from 12 to 30 Hz and the high frequency gamma band, which lies above 26 Hz.

Human voluntary movement is associated with at least two distinct types of scalp EEG changes: event-related potentials and movement related potentials. The former voltages are generated in response

to stimuli, while the latter voltages are generated with movement. There are also two distinct power changes: event-related de-synchronization or power decrease seen in both alpha and beta bands that occurs up to 2s before movement and is sustained with continuous movement, and event-related synchronization, or power increase, usually only seen in the beta band and referred to as post-movement beta synchronization, occurring at the end of movement¹⁶.

The electrodes used in recording EEG are usually organized based on the 10-20 international system. In the 10-20 international system, the distance between two adjacent electrodes are kept at 20% of the total distance between nasion, the point between forehead and nose, and inion, the bump at back of skull¹⁰. Below is an image of the electrode positioning. In the image, F, T, C, P and O are used for frontal, temporal, central, parietal and occipital areas, respectively.

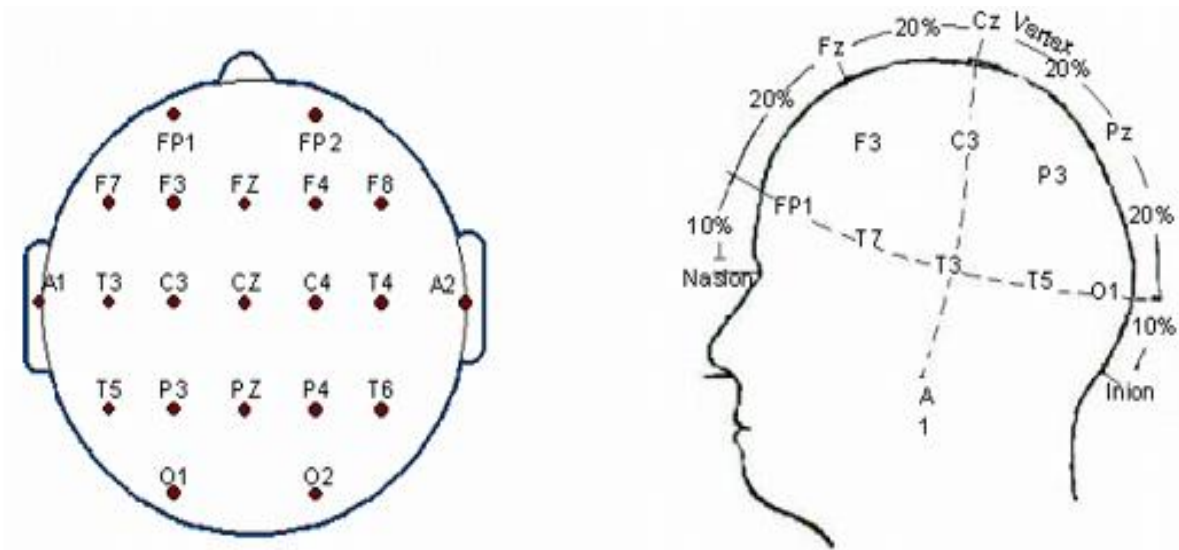


Figure 4: The 10-20 International System. From [10]

3.1.2: ECoG

ECoG signals are composed of synchronized postsynaptic potentials recorded directly from the exposed surface of the cortex. The potentials occur primarily in cortical pyramidal cells, and thus must be conducted through several layers of the cerebral cortex, cerebrospinal fluid (CSF), pia mater, and

arachnoid mater before reaching subdural recording electrodes placed just below the dura mater. ECoG samples neuronal activity from smaller cortical areas than conventional EEG. However, to reach the scalp electrodes of EEG, electrical signals must also be conducted through the skull, where potentials rapidly attenuate due to the low conductivity of bone. For this reason, the spatial resolution of ECoG is much higher than EEG^{17,18}.

3.1.3: MRI

Magnetic Resonance Imaging (MRI) is used to image every part of the body, but is particularly useful in neurological conditions, disorders of the muscles and joints, for evaluating tumors and showing abnormalities in the heart and blood vessels. In brief, MRI involves the use of three kinds of electromagnetic fields: a very strong magnetic field to polarize hydrogen nuclei, called the static field; a weaker time-varying (of the order of 1 kHz) for spatial encoding, called the gradient field(s); and a weak radio-frequency (RF) field for manipulation of hydrogen nuclei to produce measurable signals, collected through an RF antenna¹⁹. Images are usually taken every 1–4 seconds, and the voxels in the resulting image typically represent cubes of tissue about 2–4 millimeters on each side in humans.

Functional MRI measures the blood oxygen level dependent (BOLD) signal. The BOLD signal reflects vascular effects and indirectly the neuronal signal. This phenomenon is known as neurovascular coupling, and has received much attention in the last two decades. Functional MRI measures the BOLD signal with high spatial resolution and can access the whole brain. However, fMRI is highly sensitive to motion artifact and therefore requires motionlessness from the patient²⁰. Other disadvantages of fMRI include slow speed and expensive equipment.

3.2: Optical Signals

3.2.1: Slow Signal

The purpose of NIR spectroscopy (NIRS) is the in vivo quantification of the concentration of significant light-absorbing substances through the use of NIR light at different wavelengths. NIRS is the only available method for measuring the absolute concentration of deoxygenated hemoglobin (HHb) and oxygenated hemoglobin (HbO₂) in a selected part of the body in a noninvasive fashion⁶. Hemoglobin is the iron-containing oxygen-transport metalloproteinase in the red blood cells of vertebrates²².

NIRS is rooted in oximetry, which measures blood oxygenation²¹. Pulse oximetry works as follows. A sensor is placed on a thin part of the patient's anatomy and a light containing both red and infrared wavelengths is passed from one side to the other. Changing absorbance at the two wavelengths is measured, allowing determination of the absorbance due to the pulsing arterial blood alone, excluding venous blood, skin, bone, muscle and fat. A measure of blood oxygenation, the per cent of hemoglobin molecules bound with oxygen molecules, can be made based upon the ratio of changing absorbance of the red and infrared light.

Both NIRS and pulse oximetry measure changes in hemoglobin concentration levels and are therefore limited by the nature of these changes. Specifically, the concentration changes occur on a time scale on the order of seconds, and these signals are therefore termed 'slow' optical signals. However, there are three fundamental differences between NIRS and pulse oximetry. They are: (1) NIRS does not utilize visible light, which is readily absorbed by water, and therefore has better penetration than oximetry, (2) pulse oximetry considers only the arterial compartment by time gating the measurements whereas NIRS provides global assessment of oxygenation in all vascular compartments, including arterial, venous and capillary oxygenation and (3) NIRS uses more wavelengths and therefore can characterize more chromophores, or light absorbing molecules¹.

3.2.1.1: Physiology

NIRS is based on the assumption that, by studying changes in metabolism and blood circulation in the brain, one can infer whether a particular brain area is involved in the neural activity associated with a particular task. These methods are indirect in that they are mediated by neurovascular coupling, the set of biophysical and biochemical steps that occur between neuronal activity and the physiological events measured. Neurovascular coupling complicates things since it introduces a delay and it may vary with the state of the organism and the brain area¹⁴.

There are a number of physiological processes associated with neuronal activity. Bunce et al.²³ report that neuronal activity is fueled by glucose metabolism, so activity induces increases in both glucose and oxygen consumption from a local capillary bed. This stimulates the brain to increase local arteriolar vasodilation (dilation of arteries) which increases regional cerebral blood flow (rCBF) and regional cerebral blood volume (rCBV)⁴. The effect of neural activity on blood flow and volume is termed neurovascular coupling, and has received much attention in the research community over the past 10 years. Over several seconds glucose and oxygen are carried to the area via HbO₂. It is widely accepted that the degree of the increase in rCBF exceeds that of oxygen consumption, resulting in an overabundance of cerebral oxygenation²⁴.

Two major types of optical changes that occur after stimulation are 1) rapid blood deoxygenation occurring within a few seconds of stimulation and 2) a large increase in oxygenation occurring several seconds after stimulation³. The earlier slow optical effect is small deoxygenation 500ms after neuronal activation. This effect subsides within a few seconds. However, signal is small and difficult to observe noninvasively. A large increase in oxygenation begins 1.5s after neuronal activity. It is related to vasodilation and is consistent with the widely reported increase in blood flow in active cortical areas⁶. Below is an image of the general trend of oxy- and deoxygenated hemoglobin concentration levels during rest and activation.

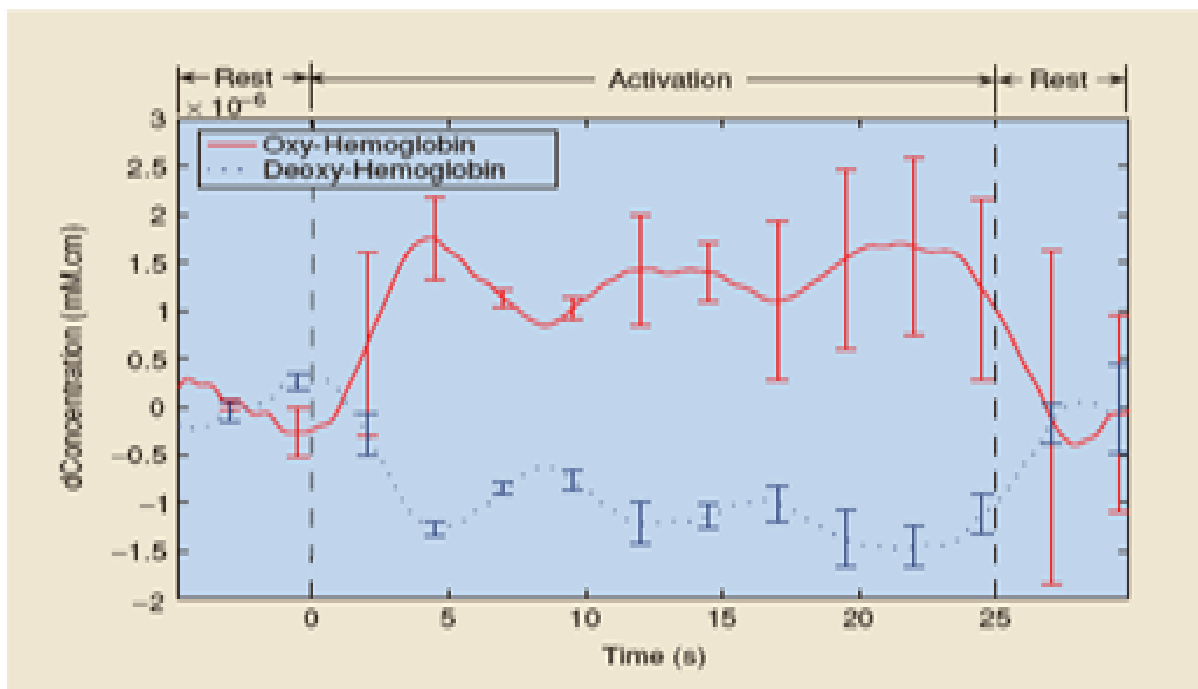


Figure 5: General trend of HHb and HbO₂ during rest and activation. From [25].

Note that the optical response to this activity is relatively easy to acquire as it leads to a 1-2% change in signal amplitude²⁶.

3.2.1.2: Calculations

The most basic setup for NIRS looks as follows

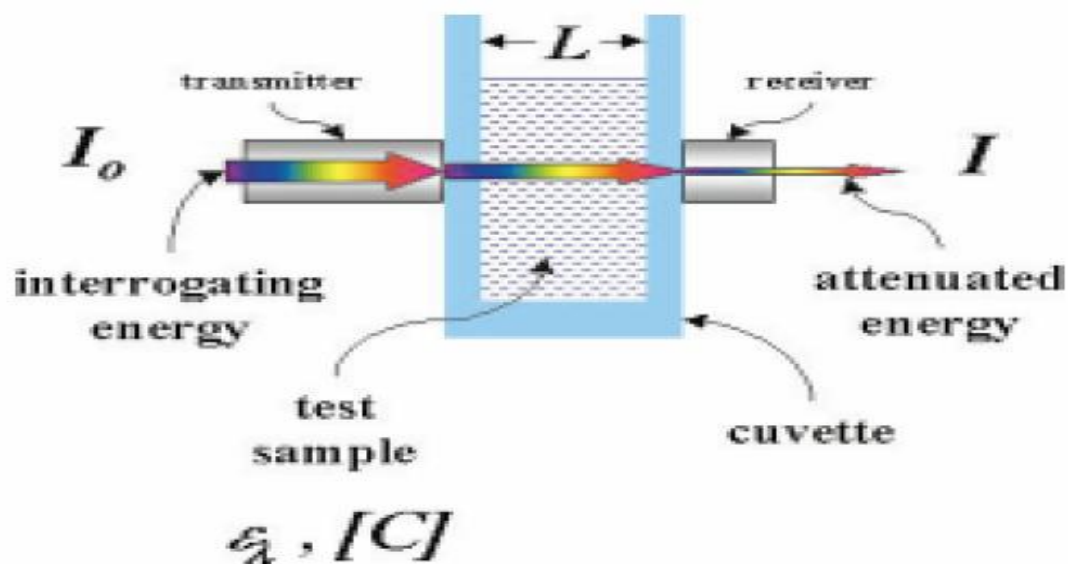


Figure 6: Simple NIRS experimental configuration. From [22]

It is assumed that nothing absorbs photon energy except the sample. In simple absorption (only 1 molecule), the energy of the arriving photon raises the molecule to an excited state, which is perceived as an increase in temperature. We then have the Beer-Lambert Law

$$I = I_0 e^{-\epsilon CL} \quad (1)$$

which gives the received intensity as a function of the input intensity in the case that there is only 1 absorbing compound in the cuvette. Here epsilon is the wavelength dependent (or energy dependent) extinction coefficient of the sample and has units $Moles^{-1}cm^{-1}$. It is important to note that I_0 is proportional to the number of injected photons per unit time, and I is proportional to the number of detected photons per unit time. Then, the wavelength-dependent attenuation, in Optical Density units (OD) is

$$A = \log(I_0/I) = \epsilon CL \quad (2)$$

We can extend equation (2) to the case where there is more than 1 absorbing compound to derive a system of equations. In this case ϵC is really a sum of products, one term for each absorbing compound.

In practice the absorption coefficient is often used as follows

$$\ln(I_0/I) = \mu_a L \quad (3)$$

In this case μ_a has units cm^{-1} . The absorption coefficient is thus also wavelength dependent. Note there is no need to list the specific absorbers when using this equation and only the absorption coefficient of the whole sample is needed. This is usually used for gases. The natural logarithm of equation (3) can easily be related to the attenuation of equation (2).

The Beer-Lambert Law (BLL) cannot be applied to tissue spectroscopy because this would require knowledge of absolute attenuation in order to calculate absolute concentrations. As tissue is highly scattering, light is attenuated by both absorption and scattering. When we include both scattering

and absorption events, the Beer-Lambert Law must be modified to add a scattering term G that related to the geometry of the tissue. We then have²¹

$$A = \log(I/I_0) = \epsilon CL\zeta + G \quad (4a)$$

or

$$A(\lambda_i) = \ln(I/I_0) = (\mu_a(\lambda_i) + \mu_s(\lambda_i)) \cdot L \cdot \zeta(\lambda_i) \quad (4b)$$

where ζ is the differential path length factor, a multiplicative factor owing to the longer path length due to scattering. Formally we have

$$A(\lambda_i, t) = \sum_{j=1}^N \epsilon_j(\lambda_i) \cdot C_j(t) \cdot L \cdot \zeta(\lambda_i) + G(\lambda) \quad (5)$$

where N is the number of attenuators. In practice, we use a reference measurement time and assume that scattering effects remain constant during measurement. Then we have

$$\Delta A(\lambda_i) = \sum_{j=1}^N \epsilon_j(\lambda_i) \cdot \Delta C_j \cdot L \cdot \zeta(\lambda_i) \quad (6)$$

This gives us a system of equations. If we use N wavelengths we can solve for ΔC for all i . Determination of ζ must be done in a laboratory setting. Its dependence on wavelength is crucial for correct results. To obtain quantitative values, the DPF has to be measured or taken from the literature. A typical value for the DPF is 6.3¹. Note that if geometrical or structural changes occur, they will be misinterpreted as changes in chromophore concentration²⁷. If we assume that only HHb and HbO₂ concentrations change, then we have 2 equations and 2 unknowns, which can be solved for the respective concentration changes. From the calculated changes in attenuation, blood oxygenation and blood volume, in μMoles , can be extracted by:

$$\begin{aligned} oxy &= \Delta c_o - \Delta c_d \\ bv &= \Delta c_o + \Delta c_d \end{aligned} \quad (7)$$

Note that tissue oxygenation refers to the amount of oxygen stored directly in the tissue (myoglobin is the typical oxygen binding protein in tissues) and cannot be monitored by NIRS. Blood oxygenation refers to oxygen saturation of the blood (with emphasis on hemoglobin).

For the BLL, we assume that the changes are homogenous in the homogenous medium. The homogeneity of changes assumption introduces two types of error: (1) the partial volume effect, which occurs because changes in the layers may be different, alters the magnitude of the changes, underestimating the focal change and (2) cross talk can mimic changes in one chromophore that are really artifacts of the changes in another. Cross talk between HHb and HbO₂ will cause an error of about 10% of the changes elicited²⁸. Presented next is a description of the cross talk effect.

In the case of inhomogeneous changes in the absorption coefficient, the total attenuation is the sum of the attenuations in each partial volume i , i.e.

$$\Delta A(\lambda) = \sum_j l_j(\lambda) \cdot \Delta \mu_{a,j} \quad (8)$$

where l_j is the partial path length in the j^{th} volume²⁹. These changes modify the measured quantities so the determined changes in the chromophores can differ from induced changes. This is the idea underlying cross talk. To illustrate this issue, consider an induced change in only one chromophore (change in a, no change in b) in a single partial volume. Then we can write

$$\varepsilon_a(\lambda_i) \cdot \Delta c_{a,ind} \cdot l(\lambda_i) = \varepsilon_a(\lambda_i) \cdot \Delta c_a \cdot L(\lambda_i) + \varepsilon_b(\lambda_i) \cdot \Delta c_b \cdot L(\lambda_i) \quad (9)$$

for each wavelength. Note here that $L(\lambda)$ has replaced $L \cdot \zeta(\lambda)$ from equation (4). Using two wavelengths in this case enables matrix inversion to be employed. Using $l^* = l/L$ we can solve

$$\frac{\Delta c_a}{\Delta c_{a,ind}} = \frac{\varepsilon_a(\lambda_1) \cdot \varepsilon_b(\lambda_2) \cdot l^*(\lambda_1) - \varepsilon_a(\lambda_2) \cdot \varepsilon_b(\lambda_1) \cdot l^*(\lambda_2)}{\varepsilon_a(\lambda_1) \cdot \varepsilon_b(\lambda_2) - \varepsilon_a(\lambda_2) \cdot \varepsilon_b(\lambda_1)} \quad (10)$$

and

$$\frac{\Delta c_b}{\Delta c_{a,ind}} = \frac{\varepsilon_a(\lambda_1) \cdot \varepsilon_a(\lambda_2) \cdot (I^*(\lambda_2) - I^*(\lambda_1))}{\varepsilon_a(\lambda_1) \cdot \varepsilon_b(\lambda_2) - \varepsilon_a(\lambda_2) \cdot \varepsilon_b(\lambda_1)} \quad (11)$$

We now define the cross talk $C_{a \rightarrow b}$ from chromophore a to chromophore b as the ratio of the determined concentration change of chromophore b and the determined concentration change of chromophore a.

Then we get for the cross talk the following:

$$C_{a \rightarrow b} = \frac{\varepsilon_a(\lambda_1) \cdot \varepsilon_a(\lambda_2) \cdot (I^*(\lambda_2) - I^*(\lambda_1))}{\varepsilon_a(\lambda_1) \cdot \varepsilon_b(\lambda_2) \cdot I^*(\lambda_1) - \varepsilon_a(\lambda_2) \cdot \varepsilon_b(\lambda_1) \cdot I^*(\lambda_2)} \quad (12)$$

Note that the crosstalk can be cancelled by using wavelengths that give the same partial path length in the medium. However, selection of such wavelengths is impractical.

In dual-wavelength analysis, equations based on the MBLL are used³⁰:

$$\begin{aligned} L \cdot \Delta C_o &= \Delta C'_o = \frac{-\varepsilon_d(\lambda_2) \cdot \Delta A(\lambda_1) + \varepsilon_d(\lambda_1) \cdot \Delta A(\lambda_2)}{E} \\ L \cdot \Delta C_d &= \Delta C'_d = \frac{\varepsilon_o(\lambda_2) \cdot \Delta A(\lambda_1) - \varepsilon_o(\lambda_1) \cdot \Delta A(\lambda_2)}{E} \end{aligned}, \quad (13)$$

$$\text{where } E = \varepsilon_d(\lambda_1) \cdot \varepsilon_o(\lambda_2) - \varepsilon_d(\lambda_2) \cdot \varepsilon_o(\lambda_1)$$

Note in this case we assume the path length is equal for both wavelengths since accurate estimation of it is almost impossible with this technique. According to the general error-propagation law, the noise levels in the hemoglobin changes depend on the differences in the hemoglobin absorption coefficients between the two wavelengths. Assuming the noise levels in the measured attenuation changes are random and independent, it can be shown that using a wavelength pair having a larger difference in the hemoglobin absorption between the two wavelengths should provide more sensitivity. However, if the difference in wavelengths is large, the assumption of equal optical path length becomes invalid.

Another problem in dual-wavelength analysis is the question of the volume of interrogation. Since the exact depth and volume of the changes are usually unknown, calculations will result in distorted spectra, i.e. wavelength A will reach more deeply into the activated area than wavelength B²⁸.

3.2.2: Fast Signal

3.2.2.1: Physiology

Villringer and Chance⁴ report that changes in optical properties have been observed in cell cultures, bloodless brain slices and intact cortical tissue. Also, they report that activity related scattering changes occur in isolated axons, neuronal cell cultures as well as in intact animals. Optical properties of isolated axons and brain slices change with neural activity. Two major phenomena underlying these changes are birefringence and changes in scattering³¹. Two possible mechanisms account for these phenomena: 1) changes are associated with repolarization of molecules within the membrane due to changes in the transmembrane potential and 2) changes are due to the movement of water associated with ion diffusion and transport, and to the consequent volume variations in intra- and extra-cellular space. Recent evidence suggests that scattering changes appear more closely related to volumetric effects. Cell swelling is a predictable physical consequence of ion movements and associated water fluxes during neural activation³². However, we still do not have a complete biophysical model of swelling and shrinking processes in neurons.

When tissue is active, movement of ions across membrane leads to changes in scattering properties¹². Scattering occurs when there is a change in refractive index: particles will scatter radiation if they have a different refractive index than the surrounding medium²¹. Scattering has two possible forms: inelastic, where incident energy is absorbed by the scatterer and energy at a different wavelength is emitted as the excited molecule falls back to alternative state. This may lead to fluorescence or phosphorescence. With elastic scattering, there is no loss of energy. Instead, re-emitted energy simply moves in a different direction. Two causes of the change in scattering properties are 1) volumetric changes associated with ion and water movement produce mechanical distension or shrinkage of the neuronal membrane and 2) changes in ion concentration in the area surrounding the membrane result in

local variations in the diffraction index. These scattering changes are believed to be at least one of the mechanisms behind fast optical signals, which occur within a couple of hundred milliseconds after stimulation. The fast changes of optical parameters are detected by averaging the time course of the activity elicited by individual stimulation³⁵. The recording of fast optical signals can be time-locked to particular events and in this case we use the term Event-Related Optical Signal (EROS)¹⁴.

Two hypotheses about the generation of the fast signals can be contrasted: the scattering hypothesis and the rapid deoxygenation hypothesis³³. No direct demonstration of the scattering hypothesis has been presented in vivo. However, if rapid deoxygenation were the cause of the fast optical signal, it should invert sign when measured using different wavelengths on the different sides of the hemoglobin isosbestic point, that is, the point where the absorption spectra of oxygenated and deoxygenated hemoglobin cross. The isosbestic point in the NIR region is around 800nm. However, this is not the case as shown experimentally, where the delay is used as the measure of fast effects. The figure below illustrates that the responses above and below the isosbestic point have the same sign.

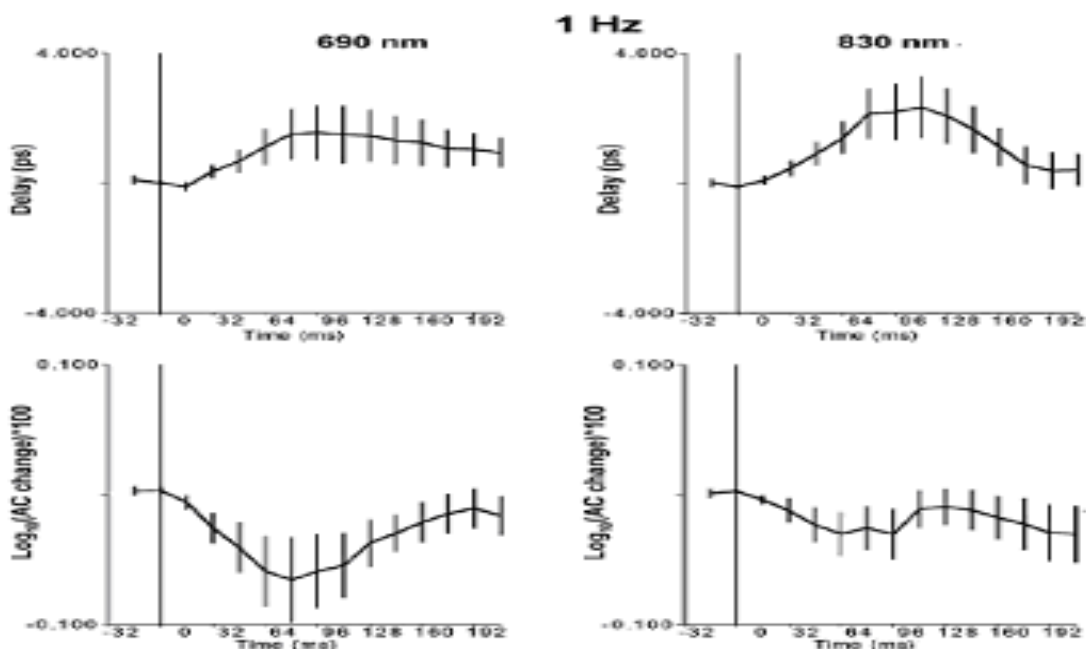
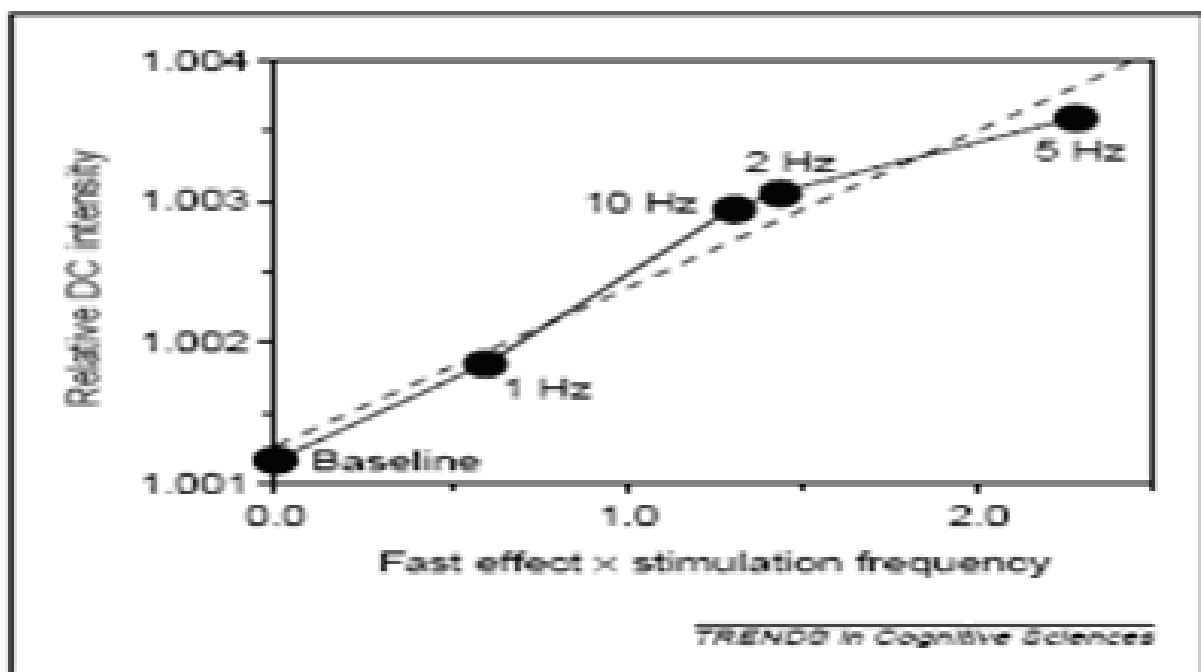


Figure 7: Evidence for Scattering Hypothesis for fast signal. From [33]

A number of experimental works have demonstrated the relationship between the fast optical signal and other recorded signals. First, Yao and George³² have shown that the fast optical response follows the integral of the electrophysiological response. Integration introduces a time lag or phase shift in a transient response waveform, but preserves the characteristic frequency of the oscillatory response. Also, Stepnowski et al. (1991) showed a linear correlation between scattered light and changes in membrane potential over a range of $\sim 200\text{mV}^{28}$. Additionally, Gratton and Fabiani¹² have shown that the fast optical signal is linearly related to the slow optical signal through the frequency of presentation of a stimulus to a subject. This result is illustrated in Figure 8. Finally, Gratton et al.³⁴ have shown that scattering changes related to neuronal events may change the signal by about .01-.1%



The relationship between fast (neurological) and slow (hemodynamic) optical signals as a function of visual stimulation frequency. The 'fast effect' was quantified as the amplitude of the EROS effect at a latency of 90 ms from stimulation (see Fig. 2a). The slow response was quantified as the amount of light reaching the detector in the period 4-14 s after the beginning of visual stimulation.

Figure 8: Relationship between fast and slow optical signals. From [12]

3.2.2.2: Challenges

EROS combines spatial resolution of better than a centimeter³ with temporal resolution of the order of milliseconds. EROS provides a higher spatial resolution than event-related potentials (ERPs) recorded electrically. With ERP, two cell populations, oriented in opposite directions, can effectively cancel each other out. This is not a problem with EROS because the responses from different locations are detected by different data channels³⁶. Also, EROS activity temporally corresponds with ERP activity and is spatially co-localized with the BOLD-fMRI response.

To demonstrate that the fast signal can be used to study the time course of neuronal activity it is necessary to meet the following criteria¹²: a) A fast signal recorded using surface instruments can be detected reliably in response to sensory stimuli and in preparation for motor activity, b) this signal is regional, i.e. it should be present only at locations where neuronal activity occurs, which should be verified using fMRI, c) the recorded activity has a time course consistent with the expected latency of neuronal activity, which should be verified using electrical recordings and d) the fast signal can be recorded in different brain areas in different tasks, and is therefore not a property of a very specific cortical region.

There are serious challenges related to the recording of the fast optical signal. Optical response due to neural firing is difficult to measure as firing yields only a .01-.1% change in signal amplitude^{26,39}. Franceschini and Boas reported averaging blocks of 1000 trials and observing only a .05% change in light intensity. It was necessary to average 700-1000 stimuli to achieve a standard error of approximately .005-.01% below the expected amplitude of the fast signal³⁸.

The relative intensity changes due to the fast signal (approximately 10^{-3}) are of one order of magnitude smaller than the relative intensity changes due to physiological effects (approximately 10^{-2}). So, Franceschini and Boas³⁸ performed various analyses to validate results and established five criteria

with which to assess the robustness of the measured signal. They are: 1) block average of signal at different wavelengths should have same temporal evolution, 2) block average of signal during rest period with a false stimulation should be flat, 3) subsets of the stimulation sequence considering only even or odd stimuli should generate a signal with the same temporal evolution as the one obtained with all of the stimuli, 4) block average of the signal during ipsilateral stimulation should be smaller than that obtained during contralateral and 5) the fast signal in the spatial maps should be localized in the hemisphere contralateral to the stimulated hand.

There are a couple of other limitations related to recording of the fast optical signal. EROS alone is insufficient to provide a complete picture of brain processes. Also, EROS does not provide information about deep brain structures as anatomical information is not provided by EROS³¹. Another limitation is that causality links cannot be proven by EROS data alone. The principal challenges for imaging of the fast optical signals are the limited dynamic range of most cameras, and the substantial noise arising from a variety of sources³². Overcoming these challenges and limitations is crucial for the development of useful systems based on fast optical signals in the brain.

CHAPTER 4: BRAIN SIGNAL PROCESSING

4.1: Introduction

Brain data analysis is based on the assumed theory of brain function, either functional specialization or functional integration. Accordingly, there are two analysis paradigms: the subtraction paradigm and the covariance paradigm⁸. In the former, event-related activity is extracted by contrasting the recorded activation to two stimuli, while the latter uncovers the temporal covariance between different brain regions during a particular task.

Recording is generally time-locked to events, and the time series obtained can be analyzed with standard methods¹⁴. Waveforms obtained for a particular stimulus/response can be averaged, cross-correlated, analyzed by wavelets or analyzed using time-frequency methods. Statistics about the reliability of the signals can be computed using standard statistical methods. When collapsing data across subjects, it is important to note that recordings from the same surface location may not correspond to the same functional cortical area across all subjects. Ignoring this issue will lead to reduction in SNR, and so several realigning/rescaling methods have been proposed. These methods require that a) the exact location of all s-d pairs must be recorded in a fixed space, which can be achieved by a 3D digitizer system, and all points must be marked on structural MR images, b) a 3D reconstruction method that is used to determine the volume from which the data are recorded, separately for each subject and c) that the 3D reconstructed data from different subjects be aligned and rescaled using one of procedures described in the literature, for example, Talairach transformation. The Talairach coordinate system is defined by making two points, the anterior commissure and posterior commissure, lie on a straight horizontal line⁴⁰. The Anterior Commissure (pre-commissure) is a bundle of white fibers, connecting the two cerebral hemispheres across the middle line, and placed in front of the

columns of the fornix. The posterior commissure is a rounded band of white fibers crossing the middle line on the dorsal aspect of the upper end of the cerebral aqueduct. Since these two points lie on a plane, the coordinate system is completely defined by requiring this plane to be vertical. In this way waveforms can be collapsed across subjects for further inspection.

4.2: General Techniques

4.2.1: Independent Component Analysis (ICA)

Amita et al.⁴¹ showed how to remove the skin blood flow artifact from recorded data. ICA transforms the experimental coordinate system into a new one that includes a non-orthogonal basis to find statistically independent components. ICA is a method for solving the blind source separation problem to find a linear coordinate system, such that the resulting signals are as statistically independent as possible⁵⁷. ICA assumes that the observed data vector $\bar{x}(t) = [\bar{x}_1(t), \dots, \bar{x}_n(t)]^T$ is a linear combination of unknown and statistically independent sources $\bar{s}(t) = [\bar{s}_1(t), \dots, \bar{s}_n(t)]^T$, for $t=1, \dots, p$. The algorithm finds a de-mixing matrix \underline{W} such that $\bar{s}(t) = \underline{W}\bar{x}(t)$. The ICA algorithm proposed by Molgedey and Schuster decomposes n-channel data into n independent components. It is non-iterative, which gives high speed, but also cannot guarantee minimization of the likelihood. MS-ICA exploits the time coherence of the source signal, and finds the de-mixing matrix by minimizing the sum-squared cross-correlations between one component at time t and another at time t+ τ across a set of time delays. They hypothesized that changes in skin blood flow and rCBF are statistically independent because their innervations are completely different. The hypothesis was then checked by consistency of the results. They focused on determining the component related to changes in skin blood flow to remove it as an artifact. To do this, they defined a new statistical value, the coefficient of spatial uniformity (CSU) as $CSU(j) = | \langle a_j \rangle / \sigma_j |$, where $\langle a_j \rangle$ is the arithmetic mean of the jth column in the mixing matrix,

and σ_j is its standard deviation. They noticed that the CSU for component 2 was the highest in all cases. Then, this component was eliminated by zeroing the corresponding column of $\underline{\underline{W}}^{-1}$ and getting the new signal $\bar{x}(t) = \underline{\underline{W}}^{-1} \bar{s}(t)$. The results are shown in the figure below.

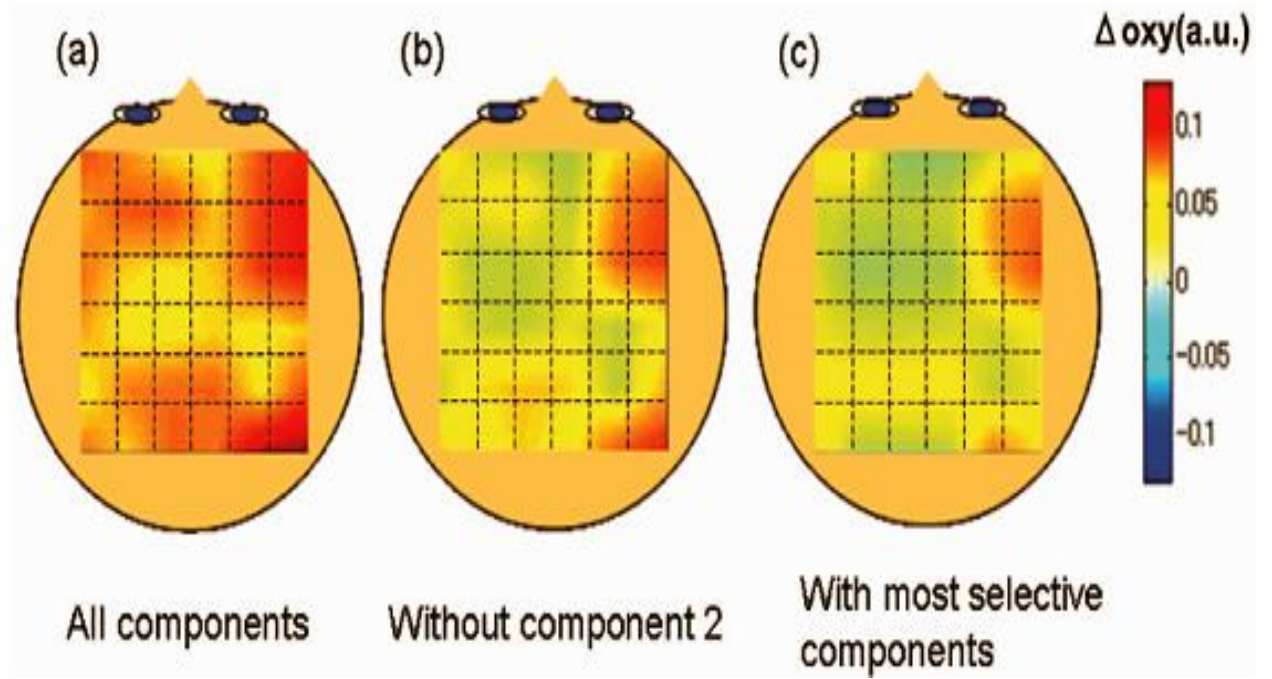


Figure 9: Illustration of ICA to remove skin blood flow component. From [41]

4.2.2: Common Spatial Patterns (CSP)

Given two distributions in high dimensional space, the supervised CSP (Common Spatial Patterns) algorithm finds directions (i.e. spatial filters) that maximize variance for one class while minimizing the variance of the other class⁴². Note that variance corresponds to power.

We have a set of trials, $\underline{\underline{S}}_i, i = 1, 2, \dots$ where each trial i is represented as a real-valued matrix of several channels (as rows, $1 \dots C$) and time points (as columns $1, \dots T$). A spatial filter $\bar{w} \in \mathfrak{R}^C$ projects these trials to the signal $\bar{w}^T \underline{\underline{S}}_i$ with only 1 channel. The formal optimization problem can be stated as follows:

$$\max_{\bar{w}} \left(\sum_{i: Trial in Class 1} \text{var}(\bar{w}^T \underline{S}_i) \right) \text{ such that } \sum_i \text{var}(\bar{w}^T \underline{S}_i) = 1 \quad (14)$$

Using the definition of variance we can restate the problem as:

$$\max_{\bar{w}} (\bar{w}^T \underline{\Sigma}_1 \bar{w}) \text{ such that } \bar{w}^T (\underline{\Sigma}_1 + \underline{\Sigma}_2) \bar{w} = 1$$

where $\underline{\Sigma}_1$ is the covariance matrix of the trial-concatenated matrix of dimension $C \times (T \text{ times number of trials in class 1})$ and similarly for $\underline{\Sigma}_2$. Note that we assume the two covariance matrices are positive definite. If they are not, we can use standard techniques for reducing the dimensionality. Now we can recast this dual optimization problem as follows. If we can calculate a matrix \underline{Q} and a diagonal matrix \underline{D} with elements in $[0,1]$ such that

$$\underline{Q} \underline{\Sigma}_1 \underline{Q}^T = \underline{D} \text{ and } \underline{Q} \underline{\Sigma}_2 \underline{Q}^T = \underline{I} - \underline{D} \quad (15)$$

Then the row vector of \underline{Q} corresponding to the highest diagonal element of \underline{D} will give the solution vector for the problem.

We proceed as follows: We have already assumed that the covariance matrices are positive definite, so that their sum is also positive definite. From matrix theory, we know that we can find an invertible matrix such that $\underline{P}(\underline{\Sigma}_1 + \underline{\Sigma}_2)\underline{P}^T = \underline{I}$. Now we define a new covariance matrix $\hat{\underline{\Sigma}}_1 \equiv \underline{P} \underline{\Sigma}_1 \underline{P}^T$ and similarly for the other covariance matrix. Then, since this new covariance matrix is also positive definite, we can use eigenvalue factorization and write $\hat{\underline{\Sigma}}_1 = \underline{R} \underline{D} \underline{R}^T$ for some orthogonal matrix \underline{R} and diagonal matrix \underline{D} . Then we can define $\underline{Q} \equiv \underline{R}^T \underline{P}$ and note that this new matrix satisfies the above problem.

Blankertz et al.⁴³ explore the question as to whether CSP-based classification can be enhanced

by preprocessing the data with a linear spatial filter (eg PCA, ICA). An arbitrary linear spatial filter can be represented by a matrix. If this matrix is invertible, the classification results will be exactly identical. On the other hand, if the matrix is not invertible, the objective of CSP analysis (on the training data) can only get worse. In addition, Hammon and de Sa⁴⁴ show that CSP works best on appropriately frequency-filtered data.

4.2.3: Common Sparse Spectral Spatial Pattern (CSSSP)

An extension of the CSP algorithm is CSSSP. The idea of new Common Sparse Spectral Spatial Pattern algorithm is to learn a complete global spatial-temporal filter in the spirit of conventional CSP. Now, we are looking for a real-valued sequence $\{b_i\}_1^T$ with $b_1=1$ such that the new trials $\underline{S}_{i,b} = \underline{S}_i + \sum_{\tau=2}^T b_\tau \underline{S}_i^\tau$ can be better classified. Note that \underline{S}_i^τ is a delayed version of the original \underline{S}_i . So, this optimization problem can be formulated as the one above as follows:

$$\max_{\bar{w}, b} \left(\sum_{i: \text{Trial in Class 1}} \text{var}(\bar{w}^T \underline{S}_{i,b}) \right) \text{ such that } \sum_i \text{var}(\bar{w}^T \underline{S}_{i,b}) = 1 \quad (16)$$

We now define $\underline{\Sigma}_y^\tau \equiv E \left(\underline{S}_i (\underline{S}_i^\tau)^T + \underline{S}_i^\tau \underline{S}_i^T \right)$ given that trial i corresponds to class y and $\underline{\Sigma}_y^0 \equiv E(\underline{S}_i \underline{S}_i^T)$. Since we can assume that, for small j , $E(\underline{S}_i^\tau \underline{S}_i^T) \approx E(\underline{S}_i^{\tau+j} (\underline{S}_i^j)^T)$, we can rewrite the problem as

$$\max_b \left(\max_{\bar{w}} \left(\bar{w}^T \left(\sum_{\tau=0}^{T-1} \left(\sum_{j=1}^{T-\tau} b(j)b(j+\tau) \right) \underline{\Sigma}_1^\tau \right) \bar{w} \right) \right) \text{ such that } \bar{w}^T \left(\sum_{\tau=0}^{T-1} \left(\sum_{j=1}^{T-\tau} b(j)b(j+\tau) \right) (\underline{\Sigma}_1^\tau + \underline{\Sigma}_2^\tau) \right) \bar{w} = 1 \quad (17)$$

With the usual CSP technique, the problem can be solved for each b . Since $b(1)=1$, a $T-1$ -dimensional problem remains which can be solved by optimization methods like gradient if T is not too large.

Consequently we get for each class a frequency band filter and a pattern. If T is large, we can add a constraint that b must be sparse. We can do this by introducing a regularization term as

$$\max_b \left(\max_{\bar{w}} \left(\bar{w}^T \left(\sum_{\tau=0}^{T-1} \left(\sum_{j=1}^{T-\tau} b(j)b(j+\tau) \right) \Sigma_1^\tau \right) \bar{w} \right) - C/T \|b\|_1 \right). \quad (18)$$

Here C is a non-negative regularization constant. With a higher C we get sparser solutions for b until at one point the usual CSP approach remains, ie, $b(1)=1$ and $b(m)=0$ for all $m>1$.

4.2.4: Dynamic Factor Analysis

The most common method of utilizing timing information to interpret connections between functional areas is based on computing the correlations between spatial units. However, the high dimensionality makes the results difficult to interpret. So, Rykhlevskaia et al.⁴⁵ explore the variation of statistics over time by applying Dynamic Factor Analysis based on the following assumptions: 1) the activity at any voxel can be completely determined by all previous activity, 2) the activity at a single voxel is an indicator of some underlying spatiotemporal component and 3) these components are temporally linked.

To this end, they experimented in the occipital area and defined 3 regions of interest, namely the primary visual cortex and left and right secondary visual cortices. The time series for each location within a given ROI were averages, and cross correlations were computed separately for each subject. Then, a covariance matrix with lag l is computed as follows:

$$\underline{\underline{\Sigma}}_l = \begin{bmatrix} \underline{\underline{\Sigma}}_{ij}(0) & \\ \underline{\underline{\Sigma}}_{ij}(l) & \underline{\underline{\Sigma}}_{ij}(0) \end{bmatrix}, \text{ for } i, j \in \{1,2,3\}$$

Note that each submatrix is a 3x3 covariance matrix, and the one with lag l corresponds to a delay of l time slots. Now, if we use PV_0 and PV_l to denote the activity in the primary visual cortex at lags 0 and l , respectively, we can construct a model with unknown coefficients that predicts the activity

at lag 1 as a function of activity lag 0. One such model is used in that publication and is called the Reticular Action Model. The coefficients can then be found using a least squares technique.

4.2.5: Wiener Filtering

A stationary process embedded in additive noise can be m.s.-optimally estimated by a Wiener smoother if the process and the noise are uncorrelated⁸. In the frequency domain the smoother can be realized as

$$W_{Wiener}(\omega) = \frac{PSD_x(\omega)}{PSD_y(\omega)} \quad (19)$$

No-stimulus intervals can be used to estimate PSD_x and activation intervals is used to estimate PSD_y .

The filtered signal can be found by $\tilde{x} = \text{Re}(iFFT(W_{Wiener} \cdot FFT(x)))$. Then the SNR gain from this

cancellation algorithm is $SNR_{gain} = 10 \text{Log}_{10} \left(\frac{AvgPower_{raw}}{AvgPower_{estimated}} \right)$

4.2.6: AR Estimation

For time-varying signals, autoregressive model estimation¹⁰ can be used to extract patterns. Signals are divided into short time segments in which the signal is assumed stationary. The segment length determines the accuracy of the estimated parameters and defines the time resolution. The AR parameters are estimated for every time segment using

$$y(t) = \sum_{i=1}^p a_i y(t-i) + e(t) \quad (20)$$

where y is the observed time series, e is a noise process and p is the model order. The LMS method can be used to determine the unknown coefficients. This simple model can be extended to the use of an external input.

4.2.7: Consistency Measures

Gratton and Fabiani⁴⁶ introduce consistency measure by computing, for each subject, the correlation of the EROS waveform with that obtained by averaging together data from all other subjects.

Formally this can be expressed by

$$r(i) = \frac{\sum_t (w(i,t) \cdot \bar{w}(t))}{\sqrt{\sum_t w^2(i,t) \cdot \sum_t \bar{w}^2(t)}} \quad (21)$$

where $w(i,t)$ is the amplitude of the response of subject i at time t , and $\bar{w}(t)$ is the average amplitude across all subjects. First Fisher transforming all consistency indices for each subject, averaging them, and then computing an inverse Fisher transform of the average value, will give an average consistency index across subjects. Then this average consistency index is a reflection of the cross-validity of the EROS waveforms.

A measure of the quality of data that can be obtained with different filtering methods can be assessed using a measure of consistency across subjects⁴⁹. This can be obtained by computing the correlation of the EROS waveform for a particular subject with the average EROS waveform across all subjects. The resulting correlations can then be averaged to obtain a measure of ‘cross-subject’ consistency of the EROS effect.

Choi et al.⁴⁷, calculated cross correlation functions as follows:

$$CCF(\tau) = \frac{\sum_t [OD(t)TS(t+\tau)]}{\sum_t TS(t)} \quad (22)$$

where OD is the optical data and TS is the tapping signal. This CCF effectively extracts the signal components that are coherent with the tapping signal. Compared to a time-triggered average, CCF yields defined values for both stimulation and rest periods. They studied the behavior of the CCF to determine that signals were not due to noise. The factor by which the level of noise is reduced by the CCF depends

on the number of data points. In contrast, a genuine signal will keep its amplitude independently of the number of data points, provided its amplitude is higher than the noise level.

Another method of measuring consistency or similarity is proposed by Zhan et al.⁴⁸. Suppose two sets of data are rescaled to zero-mean vectors. If these images are similar in spatial pattern, then one can be expressed as a linear approximation of the other. We can write

$$\vec{V}_1 = a_{12}\vec{V}_2 + \vec{e}. \quad (23)$$

Then the optimal sum-squared estimator can be found by

$$\hat{a}_{12,MSSE} = \frac{\int \vec{V}_1(t) \cdot \vec{V}_2(t) dt}{\int \vec{V}_2^2(t) dt}. \quad (24)$$

In discrete form, we find the minimum error to be

$$\tilde{\mathcal{E}}_{mix} = \frac{\mathcal{E}_{min}}{\sum_i v_1^2(i)} = 1 - r^2 \quad (25)$$

where r is the correlation coefficient between the two data sets. So, the more correlated the data, the lower the error.

One final way to measure consistency of the data, when measuring during two different sessions, is to compare the number of activated channels during each session, and to compare the location of activated channels. To this end, we define the following quantities⁵⁰:

$$R_{quantity} = 1 - |A1 - A2| / (A1 + A2) \quad (26)$$

and

$$R_{overlap} = 2 * A_{overlap} / (A1 + A2) \quad (27)$$

where $A1$ and $A2$ represent the quantity of activated channels of the first and second sessions, respectively, and $A_{overlap}$ is the quantity of identical supra-threshold channels in both sessions. The

quantity $R_{quantity}$ gives a comparison of the number of activated channels across sessions, while the quantity $R_{overlap}$ gives some measure of reproducibility of the signals.

4.3: Processing Techniques for Optical Data

Raw optical intensity data carry a number of other signals including arterial and capillary pulse ($\sim 1\text{Hz}$), respiration ($\sim 0.25\text{Hz}$) and pressure waves ($\sim 0.1\text{Hz}$)¹⁴. These signals are considerably larger than EROS. Below is an illustration of the spectrum of the intensity data.

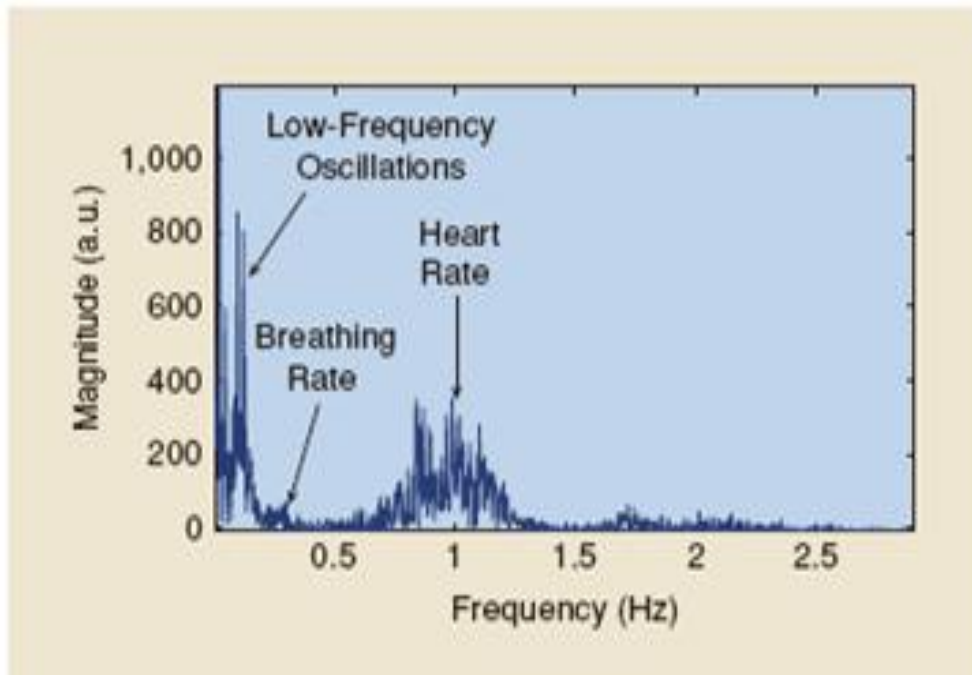


Figure FIX: Spectrum of raw intensity data. From [51]

The pressure waves are usually referred to as Mayer waves, and are spontaneous low-frequency oscillations⁵¹. Coyle et al.⁵² proposed an algorithm based on IEEE Standard 1057 to fit a sine wave to the data. They assume that the Mayer wave is of the form $m(t) = \alpha \sin(\omega t + \phi)$, and that α and ω are constant during the analysis window, which is valid provided there is no gross change in position of the user. Then, for time points $k=0, \dots, N$, the optical data y_k can be modeled by

$$y_k(A, B, C, \omega) = A \cos(\omega t_k) + B \sin(\omega t_k) + C \quad (28)$$

where $A = \alpha \sin \phi$ and $B = \alpha \cos \phi$. For a given segment of data, the four parameters can be found using a least-squares fitting approach. To account for the time-varying nature, windowed segments were used. The resulting estimate can then be subtracted from the original signal to produce a cleaned signal. An illustration of the effect of the algorithm is shown below.

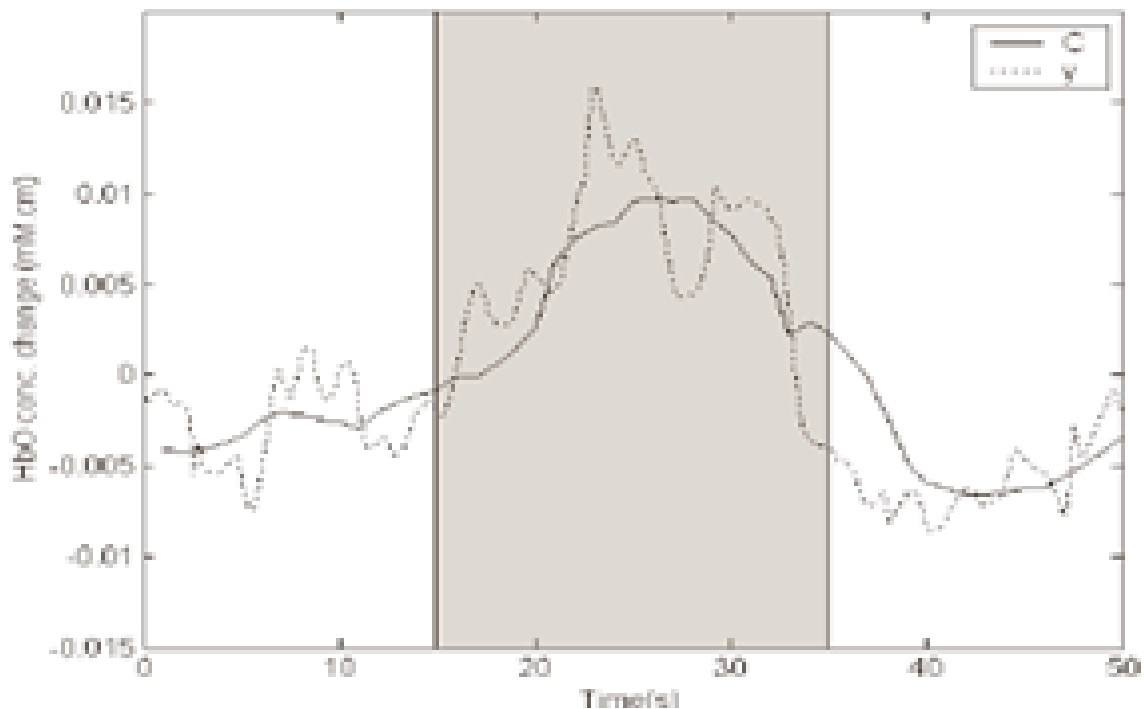


Figure 10: Effect of removal of Mayer Waves. From [52]

Gratton and Corballis⁵³ designed an algorithm for removing the pulse artifact. The procedure is based on the following assumptions: 1) Heartbeats (systoles) produce periodic increases in blood pressure (pulse), which result in periodic increases in the amount of blood flowing through the area being measured, 2) the increase in blood flow produces an increase in absorption, which will have the same periodicity as the heartbeat, 3) the residual variance in the shape of the pulse is small, 4) the wavelength and amplitude of the pulse signal may vary from trial to trial, 5) the SNR is high enough to give accurate estimates of the timing of each heart beat and 6) the phase delay between the pulse and functional phenomena is random.

On the basis of these assumptions, the average pulse can be computed by a) continuously recording the light, b) segmenting the continuous records into single beat periods, c) time-warping the single beat signal to a longer time scale and d) averaging the single beats together. The deviations between the single-beat signal and the average pulse signal can be computed by a) reversing the time warping for each beat, b) regressing the average pulse with the single-beat signal and c) subtracting the estimated contribution of the average pulse from the single-beat signal (slope only). A potential problem is the introduction of discontinuities in the signal at the boundaries between single heartbeats. To avoid this problem, the average pulse is detrended before the computation of the single-beat regressions. Note that a preliminary step for this procedure is the detection of the beginning of each heart beat. To minimize errors due to measurement noise, the beginning of each heartbeat cycle is defined as the minimum of the smoothed time derivative of the intensity signal within a particular time window following the beginning of the previous heartbeat. A problem for this procedure may occur in cases of large heart rate variability.

An example of a global cancellation algorithm is given by Brown et al.⁵⁴. With appropriate source-detector placement, they can make one channel primarily sensitive to shallow layer changes and another channel sensitive to hemodynamic changes in both shallow and deeper layers. Then, they use an adaptive FIR filter with a tapped delay line to cancel global interference. The filter is of the form:

$$e_i = y_i - \sum_{k=0}^M w_{k,i} x_{i-k} \quad (29)$$

where i is the indexed time point, y is the change in concentration measured from far s-d separations and x is the change in concentration measured from close s-d separations. Coefficients were updated using Widrow-Huff LMS algorithm by $w_{k,i} = w_{k,i-1} + 2\mu e_i x_{i-k}$. The adaptive filter converts x , the hemodynamic variation associated with the superficial layers, to an estimate of the global interferences embedded in y . Finally, the estimate is subtracted from the original time series.

Another processing method used for slow optical changes was proposed by Chance et al.⁵⁵. They model a single trial HbO₂ response by a gamma function, ie, $r_i = A_i t_i^{\alpha_i} e^{-\beta_i t_i}$, where the *i*th stimulus is presented at time *t_i*. Then the unknown parameters can be found by fitting the observed data to this

function using a least mean squares curve fitting technique: $\varepsilon = \min_{A, \alpha, \beta} \left(\left(data - \sum_{i=1}^N r_i \right)^2 \right)$. Some relevant

features that can be extracted include time-to-peak, amplitude and full width half maximum.

One final processing method that is worth mentioning can be used to extract zero-crossing and consequently phase information from voltage recording. It was proposed by McCluskey et al.⁵⁶. A typical output voltage by optical detectors is periodic with period τ . Then the amplitude and dc offset

were calculated by $V_{DC}(t) = \frac{1}{N} \sum_{k=t}^{t+10\tau} V_k$ and $V_{AC}(t) = \frac{\sqrt{2}}{N} \left[\sum_{k=t}^{t+10\tau} (V_k - V_{DC})^2 \right]^{1/2}$, where *k* is a discrete time.

To determine the phase, a zero-crossing method was used. Assuming a perfect sine wave, the signal is given by $V_t = V_{DC} + V_{AC} \sin(\omega t + \theta_t)$, where $\omega = 2\pi / \tau$. Variation in V_{DC} are small compared to V_{AVG} so that we can write $V_t - V_{AVG} \approx V_{AC} \sin(\omega t + \theta_t)$. We then define θ_n^+ and θ_n^- to be the phase values where the above crosses zero with a positive and negative slope, respectively, $\theta_n^+ = -\omega t_n^+ + 2n\pi$ and $\theta_n^- = -\omega t_n^-(2n-1)\pi$. The times were calculated using a nonlinear fit to four points. Then, the average phase value is $\theta_n = (\theta_n^+ + \theta_n^-) / 2$.

4.4: Software Packages for Optical Data Processing

Gratton⁴⁶ (2000) developed a computer program to produce maps of the (phase) optical response for each data point and overlay them over sample images of the surface of the cortex. The same program

allows for deriving statistical analyses across subjects for each data point, or for preset intervals and for plotting the data according the Talairach coordinates.

Another software package useful for processing optical data is P-POD³⁶ (Pre-Processing of Optical Data; Matlab). This included 1) correction of phase 2) baseline correction 3) correction of pulse artifacts (Gratton and Corballis) and 4) averaging. Averages are low-pass filtered with 100% roll-off between 10 and 15 Hz and a filter length of 49 data points. Average waveforms are computed for each channel, participant and condition.

CHAPTER 5: Path of Light in the Brain

5.1: Introduction

Head tissues vary considerably with respect to their optical properties¹⁴. For example, bone has a relatively high scattering coefficient but low absorption compared to gray matter. The cerebrospinal fluid (CSF), a thin layer around and inside the brain, is almost transparent to light, but the subarachnoid space in which it is contained contains dense webs of blood vessels. So, NIR light can travel without much resistance in a direction perpendicular to the surface but can travel very little in a direction parallel since it will be absorbed. The opposite occurs with white matter, which has a very high scattering coefficient and whose effect is to reflect most of the light reaching it.

Because the movement of photons in the head is random, there is no preferred direction. If the medium was infinite and homogenous, the movement of the photons could describe a sphere. However, in reality, the diffusive tissue is surrounded by non-diffusive air. In this situation, photons that are very close to the surface are likely to move outside the diffusive medium. Once they enter the non-diffusive medium, their movement becomes rectilinear³. Below is a sample trajectory of photons injected by a source located 3 centimeters from a detector.

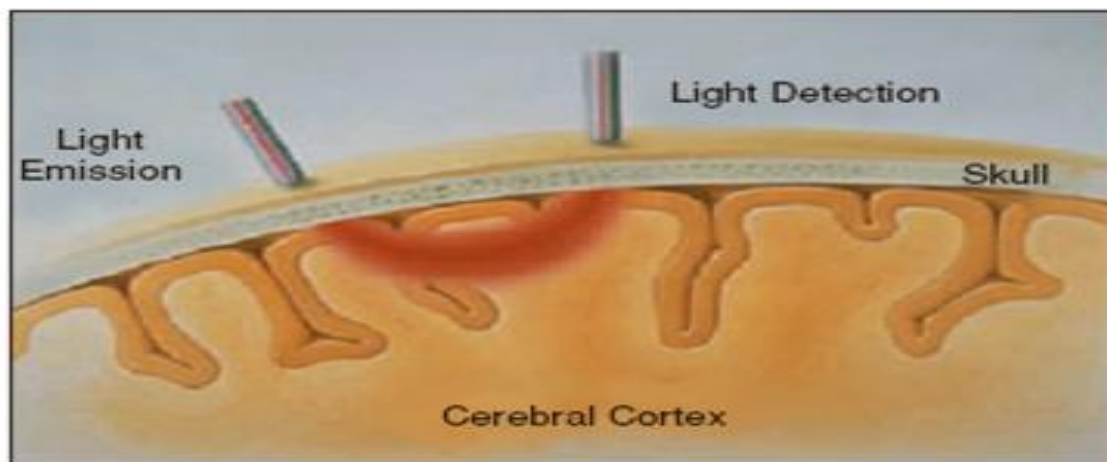
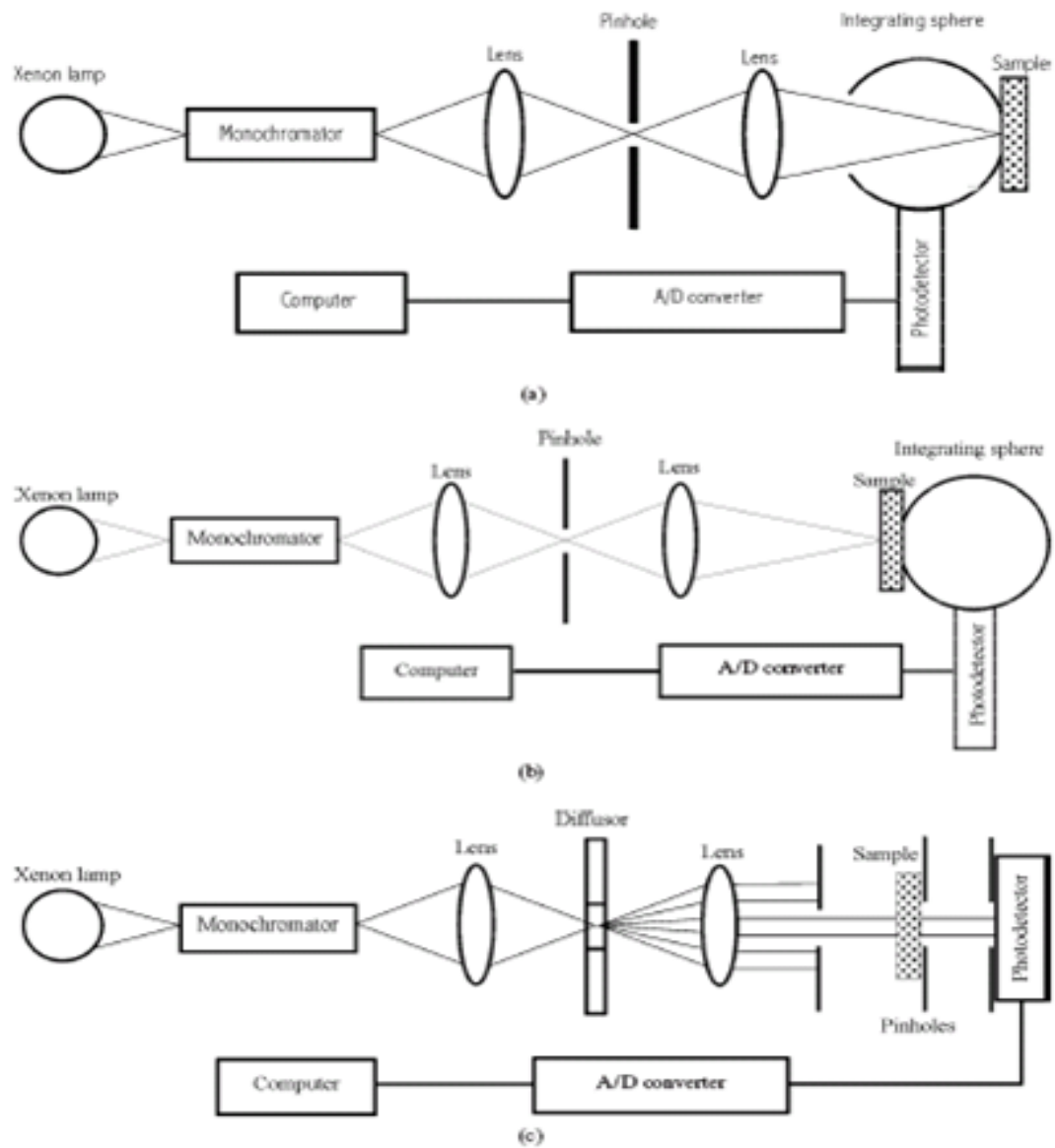


Figure 11: Sample trajectory of photons. From [23]

There exist two classes of methods for measuring optical properties of tissue⁵⁸. In direct techniques, optical properties are found using nothing more complicated than the Beer-Lambert Law. Unscattered transmission measurements and effective attenuation measurements are examples of direct methods. In indirect techniques, a theoretical model of light scattering is used. This method can be subdivided into iterative and non-iterative methods. In indirect iterative methods, the optical properties are implicitly related to measured quantities. The values of the optical properties are iterated until the calculated transmission and reflection match the measured values. These methods are the most cumbersome but also allow the most flexibility. Some examples are diffusion theory, adding-doubling models and Monte Carlo methods. Indirect non-iterative methods use equations in which the optical properties are explicitly given in terms of the measured quantities. An example of this type is the time-of-flight technique, in which a short light pulse is used instead of a continuous wave. All of the aforementioned types of methods are prone to the following sources of error: 1) physiological condition of the biological sample 2) irradiation geometry 3) boundary index mismatching 4) numerical apertures in the sensing fibers 5) angular resolution of the detectors 6) separation of forward scattered and unscattered light and 7) theory used for the inverse problem of finding optical parameters based on experimental data.

5.2: Tissue Optical Properties via Experiment

There are several tissue optical parameters that can be measured via experiment. Diffuse reflectance, total transmittance and collimated transmittance can be measured using an integrating sphere. From these experimental data, the optical parameters can be determined using an inverse Monte Carlo technique. Monte Carlo will be addressed in section 5.4.



Experimental configurations for (a) diffuse reflectance measurement, (b) total transmittance measurement and (c) collimated transmittance measurement.

Figure 12: Experimental Configuration for single integrating sphere. From [59]

Pickering et al.⁶⁰ introduce the double integrating sphere technique for measuring the optical properties of tissue.

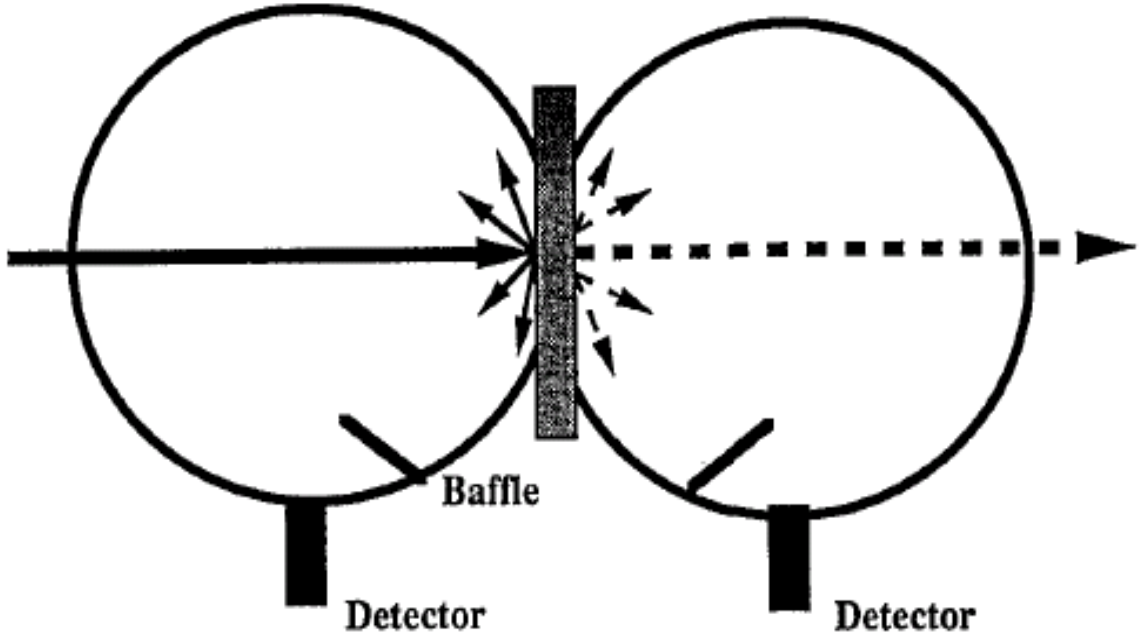


Figure 13: Double integrating sphere configuration. From [60]

Note that there is a baffle in each sphere to block the detector from the light that comes directly from the sample. The left sphere is called the reflectance sphere, while the right sphere is called the transmittance sphere.

For collimated light incident on the sample we have the following expressions for power in the reflectance and transmittance spheres, respectively:

$$\begin{aligned}
 V_{REF,\%} &= \left(\frac{V - V_0}{V_r - V_{r0}} \right)_{REF} = \frac{b_{1r} [(R_c + \alpha_r R_{cd})(1 - b_{2t} R_d) + \alpha_r b_{2t} T_d (T_{cd} + m_t T_c)]}{(1 - b_{2r} R_d)(1 - b_{2t} R_d) - b_{2r} b_{2t} T_d^2} \\
 V_{TRA,\%} &= \left(\frac{V - V_0}{V_r - V_{r0}} \right)_{TRA} = \frac{b_{1t} [(T_c + \alpha_t T_{cd})(1 - b_{2r} R_d) + \alpha_t b_{2r} T_d (R_{cd} + m_r R_c)]}{(1 - b_{2r} R_d)(1 - b_{2t} R_d) - b_{2r} b_{2t} T_d^2}
 \end{aligned} \quad (30)$$

where V is the voltage at the detector with the sample, V_0 is the voltage without the sample, V_r is the voltage with a reference plate instead of the sample and V_{r0} is the background measurement with no reference plate, using only a single sphere and adjusting the geometry as necessary. Also, R_d is the

diffuse reflectance of the sample for diffuse irradiance, R_c is the unscattered reflection of the sample for collimated irradiance and R_{cd} is the diffuse reflectance of the sample for collimated irradiance. Note the three transmittances are defined similarly as the reflectance. For the sphere parameters we have that α is the fraction of the total sphere area that is occupied by the sphere wall, m is the diffuse reflectance factor of the sphere wall, and the b 's are constants. Note that these equations account for losses through absorption by the walls and losses through the apertures. However, some light will move back and forth between the spheres which continues until all of the light has been absorbed or lost. This coupling of reflection and transmission coefficients implies that they cannot be determined analytically from the measurement of the sphere powers for either of the incident light geometries.

The equations have 6 parameters and 6 unknown coefficients. The measurement of the collimated transmittance with a third detector at a distance from the second sphere yields T_c :

$$T_c = \frac{V_c - V_{c0}}{V_{cr} - V_{cr0}} = V_{c\%}, \text{ where } V_c \text{ is the voltage recorded with the sample in place between the spheres,}$$

V_{cr} is the voltage recorded without the sample and $V_{c0} = V_{cr0}$ is the background signal with the source extinguished. The specular reflection R_c may be calculated from Fresnel's equations. Note that R_{cd} is a special case of R_d and so some models, such as adding-doubling, are able to couple these coefficients leaving only 2 unknown coefficients with 2 equations. So, after determining the sphere constants, we can solve for all unknown coefficients.

The sphere parameters can be found most easily with diffuse irradiance. If no sample is present,

$$V_{\%} = b_1. \text{ By using a standard of known reflectance, we have } b_2 = \frac{b_1 - V_{\%}}{V_{\%} R_{ds}}, \text{ where } R_{ds} \text{ is the known}$$

diffuse reflectance of the standard. Also, using A_s as the sample areas and A as the inner surface area of the sphere, we have

$$m = \frac{-\frac{A_s}{A} + b_2}{\alpha b_2} \quad (31)$$

Lu et al.⁶¹ discusses the effect of light losses between the two integrating spheres.

5.3: Transport Theory

Photon transport in biological tissue can be equivalently modeled numerically with Monte Carlo simulations or analytically by the radiative transfer equation (RTE)⁶². However, the RTE is difficult to solve without introducing approximations. A common approximation summarized here is the diffusion approximation. Overall, solutions to the diffusion equation for photon transport are more computationally efficient, but less accurate than Monte Carlo simulations.

5.3.1: Radiative Transfer Equation (From [62])

The flow of radiation energy through small area can be characterized by radiance L , a function of position vector r , unit direction vector s and time, which has units Watts (energy) per unit normal area per second per unit solid angle.

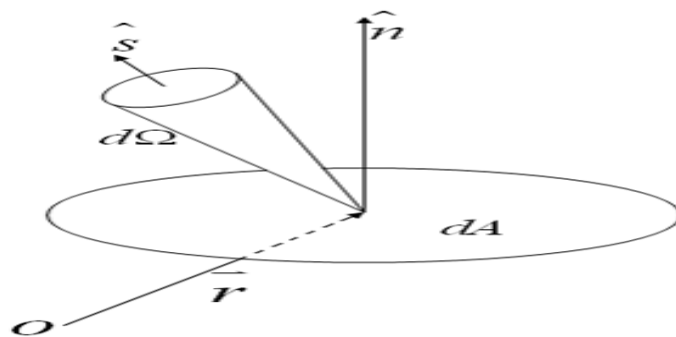


Figure 14: Schematic of energy flow through a differential area element. From [62]

The RTE is a differential equation describing radiance $L(\vec{r}, \hat{s}, t)$. Briefly, the RTE states that a beam of light loses energy through divergence and extinction and gains energy from light sources in the medium and scattering directed towards the beam. Coherence, polarization and non-linearity are neglected. Optical properties such as refractive index n , absorption coefficient μ_a , scattering coefficient

μ_s , and scattering anisotropy g are taken as time-invariant but may vary spatially. Scattering is assumed to be elastic. The RTE is thus

$$\frac{\partial L(\vec{r}, \hat{s}, t)/c}{\partial t} = -\hat{s} \cdot \nabla L(\vec{r}, \hat{s}, t) - \mu_t L(\vec{r}, \hat{s}, t) + \mu_s \int_{4\pi} L(\vec{r}, \hat{s}', t) P(\hat{s}', \hat{s}) d\Omega' + S(\vec{r}, \hat{s}, t) \quad (32)$$

where c is speed of light in tissue, $\mu_t = \mu_a + \mu_s$ is the extinction coefficient, S describes the light source, P is a phase function representing the probability of light with propagation direction \hat{s}' being scattered into solid angle $d\Omega$ around \hat{s} . In the RTE, six different independent variables define the radiance at any spatial and temporal point (x , y , and z from \vec{r} , polar angle θ and azimuthal angle ϕ from \hat{s} , and t).

The phase function describes the angular distribution of a single scattering event. For tractability, the phase function is assumed to be a function of only the angle between two vectors⁵⁸. If the integral of the phase function is normalized, ie, $\int_{4\pi} p(s \cdot s') d\omega' = 1$, then $p(s, s')$ is the probability density function for scattering from direction s' to direction s . Usually the form of the phase function is not known. The Henyey-Greenstein scattering phase function is a valid phase function approximation for brain tissues⁵⁹.

Sine these functions are complicated, the phase function is usually characterized by a single parameter g called the average cosine of the phase function. Then, $g = \int_{4\pi} p(s \cdot s')(s \cdot s') d\omega'$. This parameter is sometimes called the anisotropy coefficient.

The g -factors increase with increasing wavelength¹¹. One possible explanation for this is that there is a sizable amount of Rayleigh scattering present, which lowers the value of g . Rayleigh scattering occurs when light hits molecules with radius r , which is much less than the wavelength of light²¹. Since Rayleigh scattering falls off like $1/\lambda^4$, the contribution of small particle scattering to the g -factor will decrease with wavelength.

5.3.2: Diffusion Approximation

By making appropriate assumptions about the behavior of photons in a scattering medium, the number of independent variables can be reduced. These assumptions lead to the diffusion theory (and diffusion equation) for photon transport⁶². Two assumptions permit the application of diffusion theory to the RTE are 1) relative to scattering events, there are very few absorption events (ie, $\mu'_s \gg \mu_a$) Likewise, after numerous scattering events, few absorption events will occur and the radiance will become nearly isotropic. This assumption is sometimes called directional broadening and 2) In a primarily scattering medium, the time for substantial current density change is much longer than the time to traverse one transport mean free path. Thus, over one transport mean free path, the fractional change in current density is much less than unity. This property is sometimes called temporal broadening. Then, the (time-dependent) diffusion approximation is

$$\frac{\partial \Phi(\vec{r}, t)}{c \partial t} + \mu_a \Phi(\vec{r}, t) - \nabla [D \nabla \Phi(\vec{r}, t)] = S(\vec{r}, t), \text{ where } D = \frac{1}{3(\mu_a + \mu'_s)} \quad (33)$$

The typical value² for μ'_s is around 1 mm^{-1} whereas the absorption coefficient is usually between .005 and $.02 \text{ mm}^{-1}$. This gives some validity to the use of the diffusion approximation. Note also that since $\mu'_s \gg \mu_a$, we can use the approximation $D \approx \frac{1}{3\mu'_s}$.

It is important to note that the diffusion approximation is only valid in highly scattering media. Since the CSF is not highly scattering, results using the diffusion approximation are not valid in this region. So, some researchers have utilized Radiosity Theory in the CSF layer, while maintaining the diffusion approximation in all other layers. Simulations of this sort are discussed in the Finite Element Method section of this paper.

5.3.3: Photon Density

When working in the frequency domain, it is useful to think of light propagating in a turbid medium in term of photon density waves³⁵. In 1993, Fishkin and Gratton derived the following

expression for a photon density wave at a detector valid in the diffusion regime in an infinite and homogenous medium.

$$U(r,t) = \frac{S}{4\pi v D r} \left(e^{-r(\mu_a/D)^{1/2}} + A e^{-kr} e^{i(\phi_0 - \omega t)} \right) = U_{DC} + U_{AC} e^{i(\phi_0 - \omega t)} \quad (34)$$

where r is the source-detector distance, ω is the angular modulation frequency, v is the speed of light in the medium, $k = [(v\mu_a - i\omega/vD)]^{1/2}$, ϕ_0 is the phase of the source, A is its modulation depth, S is the strength and $D = 1/\mu_s'$. From this equation, we can derive the following quantities:

$$\begin{aligned} \phi &= r \left(\frac{\mu_a}{2D} \right)^{1/2} \left[(1+x^2)^{1/2} - 1 \right]^{1/2} \\ \ln(rU_{DC}) &= r \left[- \left(\frac{\mu_a}{D} \right)^{1/2} \right] + \ln \left(\frac{S}{4\pi v D} \right) \quad (35) \\ \ln(rU_{AC}) &= r \left[- \left(\frac{\mu_a}{2D} \right)^{1/2} \right] \left[(1+x^2)^{1/2} + 1 \right]^{1/2} + \ln \left(\frac{S}{4\pi v D} \right) \end{aligned}$$

$$\text{where } x = \frac{\omega}{v\mu_a}$$

We can denote the slopes of the three above equations as S_ϕ , S_{DC} and S_{AC} , respectively. Using any pair of these slopes we can derive the values of the absorption and reduced scattering coefficients as follows:

$$\text{Using DC and phase we have } \mu_a = \frac{-\omega S_{DC}}{2v S_\phi} \left(\frac{S_\phi^2}{S_{DC}^2} + 1 \right)^{-1/2} \quad \text{and} \quad \mu_s' = \frac{S_{DC}^2}{3\mu_a} \quad (36)$$

$$\text{Using AC and phase we have } \mu_a = \frac{\omega}{2v} \left(\frac{S_\phi}{S_{AC}} - \frac{S_{AC}}{S_\phi} \right) \quad \text{and} \quad \mu_s' = \frac{S_{AC}^2 - S_\phi^2}{3\mu_a} \quad (37)$$

$$\text{Using DC and AC we have } \mu_a = \frac{\omega}{2v} \frac{S_{DC}}{S_{AC}} \left(\frac{S_{AC}^2}{S_{DC}^2} - 1 \right)^{-1/2} \quad \text{and} \quad \mu_s' = \frac{S_{DC}^2}{3\mu_a} \quad (38)$$

Although these equations are valid in an infinite medium, similar equations can be written for a semi-infinite medium. The diffusion approximation is based on using the photon density, which can be

interpreted as a quantity proportional to the probability of finding a photon at a distance r from the source at time t . It can be shown that at large enough distances from the light source and at frequencies below 1GHz the photon density obeys the diffusion equation⁶⁴.

Another quantity representing the photon density is the photon measurement density function⁶³. The PMDF describes how sensitive a measurement is to different points in the tissue. For intensity measurements, the PMDF at position p for a source at s and measurement of a change in fluence at position m is $J_{\Gamma}(p, m, s) = \Delta\Gamma(m) / \Delta\mu_a(p)$. For mean time the PMDF is $J_{\langle t \rangle}(p, m, s) = \Delta\langle t \rangle(m) / \Delta\mu_a(p)$.

5.4: Simulation Methods

5.4.1: Monte Carlo Methods

In practice, the spatial sensitivity profile, that is, the path travelled by the photons, can be predicted by Monte Carlo simulation⁶⁵. In this method, photons with unit weight are injected one-by-one into the model used for the head. The model may be homogenous, layered or more complex. An example of a sophisticated head model is given below.

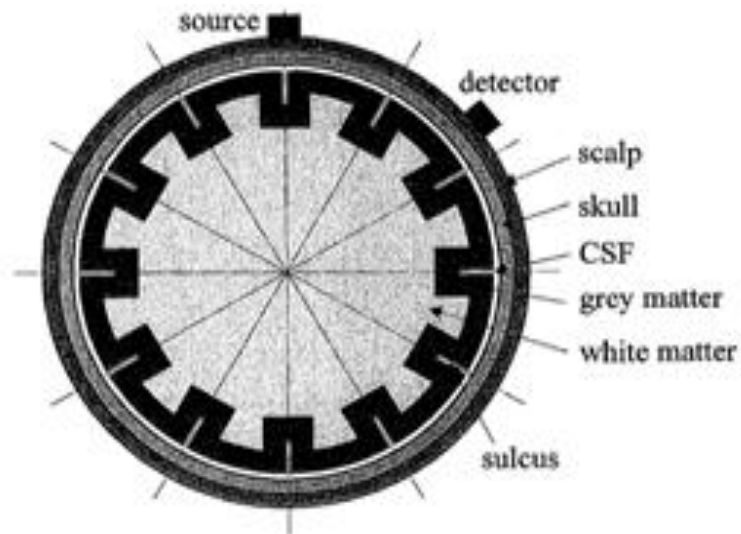


Figure 15: Schematic of a sophisticated head model. From [65]

The propagation of a photon is determined by the transport scattering coefficient of the tissue and a random number. The random number is the essence of simulating a diffusion process. The successive scattering lengths l are determined by $l = -\ln R / \mu'_{s,i}$, where i indicated tissue type and R is a random number. If a photon crosses a boundary between layers, then the scattering length must be corrected. Scattering angles are calculated from random numbers. When the photon is scattered out of the model, the ultimate survival weight W of the photon is calculated by $W = W_0 \sum_i \exp(-\mu_{a,i} L_i)$. In the case where a photon arrives at a detector, the photon trajectory is weighted by the survival weight and is accumulated into a matrix to calculate the SSP. Presented below are spatial sensitivity profiles predicted by Monte Carlo simulation.

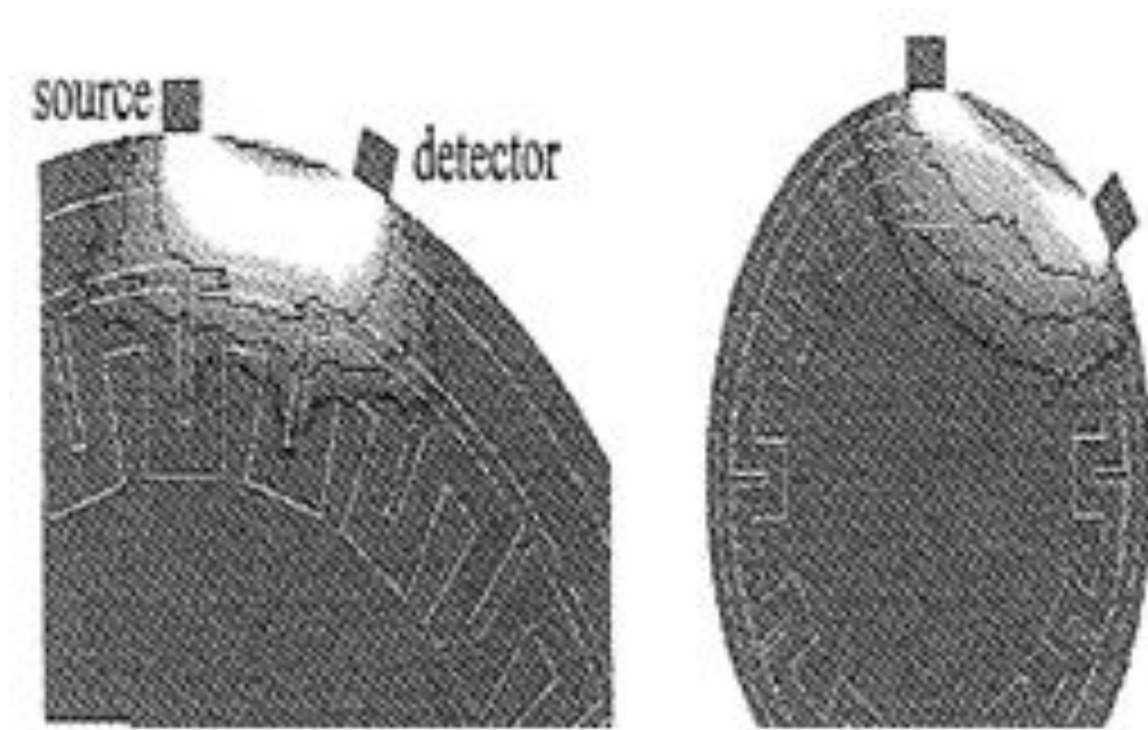


Figure 16: Spatial sensitivity profiles for sophisticated head models.

Right is an adult head model and left is a neonatal head model. From [65]

It is clear from the previous figure that photons travel a curved path through the head. When the source and detector are placed 30mm apart, very little, if any, light makes it into the white matter. For the adult head, most of the light travels in the gray matter. For the neonatal head model, most of the light travels in the CSF. It should be noted that this simulation was based on the diffusion approximation. As the approximation is only valid in regions with high scattering coefficients, light paths in the CSF are erroneously calculated. This issue is addressed in the next section.

Obrig et al.⁶⁶, motivated by the fact that they could not measure the fast signal experimentally, ran Monte Carlo simulations to estimate the expected changes in the adult head. According to this estimation the magnitude of the effect is so small that the noise level is generally greater than the signal itself. This makes it very difficult to measure the fast optical signal. Steinbrink et al.⁶⁷ also questioned the measurability of the fast optical signal. They noted that intensity changes on the exposed hippocampus of the cat following collateral electrical stimulation have been reported. The largest reported was an intensity change of .1%. To derive an expected scatter change from this intensity change a Monte-Carlo simulation was performed. Regarding the estimation of the amplitude of scattering changes the results are as follows:

The background optical properties assumed for the MC-study and the related proportionality factor k

Run	d' of layer in mm	μ_a in 1/mm	μ_s' in 1/mm	g	k
1	Inf	0.01	10	0.9	0.9
2	Inf	0.01	3	0.7	1.0
3	Inf	0.03	10	0.9	0.9
4	Inf	0.01	5	0.9	0.8
5	0.2	0.01	10	0.9	4.0

A proportionality factor 0.9 indicates that an intensity change of 0.1% can be explained by a change in μ_s of 0.09%. Note that assuming a change in a thin layer only (run 5) returns a larger proportionality factor.

Figure 17: Explanation of fast effects in relation to scattering changes. From [67]

where runs 1-4 used a homogenous model and run 5 used a heterogeneous one. This shows that the largest reported change of .1% change in intensity corresponds to a scatter not larger than .4%.

To simplify the overall analysis, they defined a fractional sensitivity factor for intensity changes. For intensity changes we define $k_I = ((\Delta I / I)(\Delta \mu'_s / \mu'_s))$, which relates scatter changes in percent to fractional intensity changes. For time of flight we define $k_{\langle t \rangle} = (\Delta \langle t \rangle) / (\Delta \mu'_s / \mu'_s)$ which is given in ps/%.

The sensitivity factors of intensity K_I and mean time of flight $K_{\Delta \langle t \rangle}$ calculated by a Monte-Carlo simulations for a scattering change of different spatial extent

Location of change in μ'_s	d in mm	Inhomogenous model		Homogenous model	
		K_I	$K_{\Delta \langle t \rangle}$ in ps/%	K_I	$K_{\Delta \langle t \rangle}$ in ps
(A) Total gray matter	5	0.06	0.07	0.04	-0.06
(B) Layer in gray matter	1	0.05	0.04	0.02	-0.02
(C) Gray and white matter	Inf.	0.04	0.03	-0.02	-0.07

If one assumes a scattering change of 0.1% in the gray matter (case A) the resulting change in the optical signal corresponds to $\Delta I / I = 0.006\%$ and $\Delta \langle t \rangle = 0.007$ ps.

Figure 18: Estimated effect of scattering changes. From [67]

They thus conclude an intensity sensitivity factor of .1% change in intensity per percent change in reduced scattering, and a sensitivity factor of mean time of flight of about .1ps per percent change in reduced scattering. Thus, a scatter change of .1% leads to an upper limit change in intensity of .01% and a change in mean time of flight of .01ps. However, in practice, the rough topographical positioning will produce a partial volume effect reducing these factors. Also, these estimates are based on invasive stimulation which may reduce the intensity change by an order of magnitude. Therefore, in practice, the

.1% change in scatter in the cerebral cortex corresponds to a .0001% for changes in intensity and .001ps for changes in mean time of flight.

5.4.2: Finite Element Methods

Light propagation in a high-scattering tissue can be described by the time-independent diffusion equation. The FEM can be employed to solve it⁶⁸. The domain of the scattering tissue Ω of which boundary is $\partial\Omega$ is divided into elements, which are joined at D vertex nodes. The solution of photon density $\Phi(\vec{r})$ is approximated by a piecewise polynomial function $\Phi^h(\vec{r}) = \sum_{i=1}^D \Phi_i u_i(\vec{r})$ where $u_i(\vec{r})$ are linear nodal shape functions. The calculation of standard FEM can be expressed as $\underline{\underline{F}}\underline{\underline{\Phi}} = \underline{\underline{q}}_0$, where $\underline{\underline{F}}$ is the system matrix, $\underline{\underline{\Phi}}$ is the photon density matrix and $\underline{\underline{q}}_0$ is the source vector. The system matrix is given by $\underline{\underline{F}} = \underline{\underline{K}} + \underline{\underline{C}} + \zeta \underline{\underline{A}}$ where

$$\begin{aligned} K_{ij} &= \int_{\Omega} \kappa(\vec{r}) \nabla u_i(\vec{r}) \nabla u_j(\vec{r}) d^2 \vec{r} \\ C_{ij} &= \int_{\Omega} \mu_a(\vec{r}) u_i(\vec{r}) u_j(\vec{r}) d^2 \vec{r} \quad (38) \\ A_{ij} &= \int_{\partial\Omega} u_i(\vec{m}) u_j(\vec{m}) d\vec{m} \end{aligned}$$

and ζ is a constant determined by the boundary condition. Note that $\kappa(\vec{r}) = 1/3\mu'_s(\vec{r})$.

In the presence of a low scattering region Ω_L in the model, a modification in the calculation process must be made. The modification comes from the internal source terms on the low-scattering boundaries as follows: $\underline{\underline{E}}\underline{\underline{\Phi}} = \underline{\underline{q}}_0(\Omega_L)$, where the coupling matrix $\underline{\underline{E}}$ has components

$$E_{ij} = \zeta \int_{\partial\Omega_L} u_i(\vec{m}) \int_{\partial\Omega_L} u_j(\vec{m}') f_{\vec{m},\vec{m}'} d\vec{m} d\vec{m}' \quad (39)$$

where f is the transmittance and reflectance ratio from \bar{m} to \bar{m}' in the low-scattering region. Then we have $(\underline{F} - \underline{E})\Phi = \bar{q}_L$. The outgoing flux, which represents the intensity of the detected light at position \bar{r} on the surface of the head model can be given by

$$\Gamma_0(\bar{r}) = -\kappa(\bar{r})\hat{n} \bullet \nabla\Phi(\bar{r}) \quad (40)$$

where $\kappa(\bar{r}) = 1/\mu_s'(\bar{r})$. The transmittance and reflectance ratios are obtained from the analysis of light propagation in the low-scattering region predicted by Monte Carlo. If a photon reaches the boundary between the high- and low-scattering regions, the survival weight of the photon closest to \bar{m}' is then $W(\bar{m}, \bar{m}') = \exp(-\mu_{a,low}l)$. The survival weight is accumulated with respect to each node and is normalized by the sum of the initial weight of incident photons to obtain the transmittance and reflectance ratios.

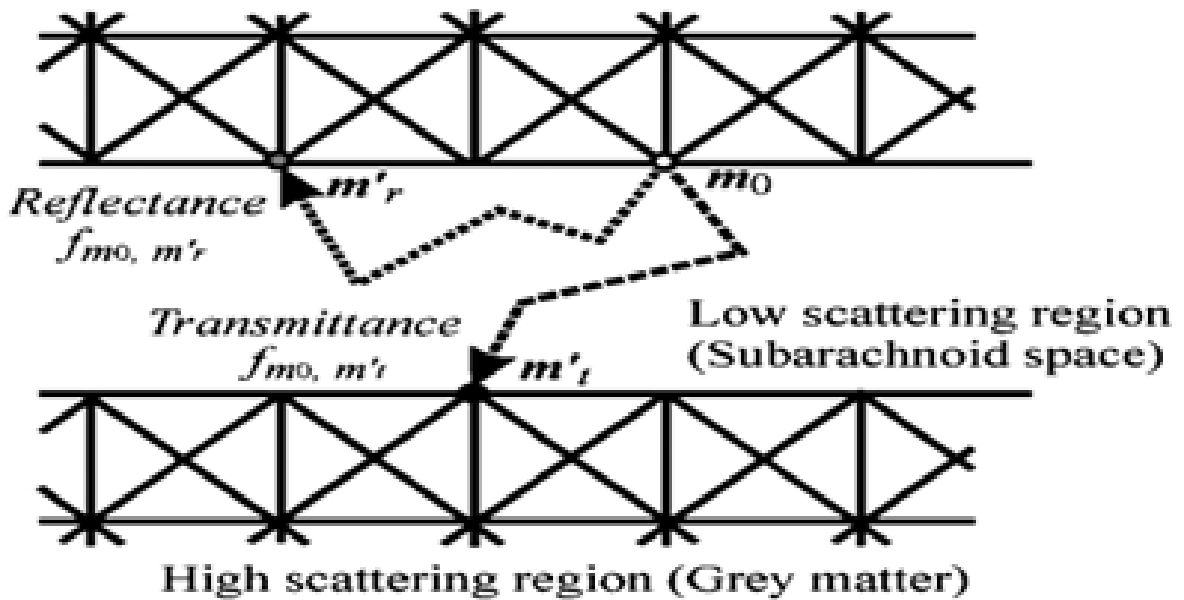


Figure 19: FEM calculation between low- and high-scattering regions. From [68]

Another method for incorporating the low-scattering CSF in simulation is the radiosity-diffusion method⁶⁹. The idea is to calculate light propagation in the scattering medium by the diffusion equation (FEM) and in the non-scattering region by radiosity theory. The results by the two methods are

combined in an iterative scheme until there is a minimum change in the flux at the boundary between scattering and non-scattering media. An improvement would be seen if the model enabled the effect of discrete absorbers and scatters in the CSF.

It is worth noting the computational effort required to simulate photon transport in tissue. On a SunSparc 20 workstation, calculations take ~200-h CPU time for the Monte Carlo Method, 3-min for the FEM based on the diffusion theory and 15-min for the FEM based on the hybrid radiosity-diffusion theory.

CHAPTER 6: OPTICAL INSTRUMENTATION

6.1: Sources and Detectors

There are a variety of NIR optical sources that are used to interrogating tissue. The sources differ in a number of ways, including bandwidth, output power and cost²¹. For example, low-cost light emitting diodes (LEDs) have been used in a number of studies. LEDs have a 50nm full-width maximum spectral bandwidth and an output power of 2-10mW. On the other hand, laser diodes have a 5nm bandwidth and an output power of 10W. A super-luminescent diode (SLD) falls in between LEDs and laser diodes. It has a high power output and relatively low coherence.

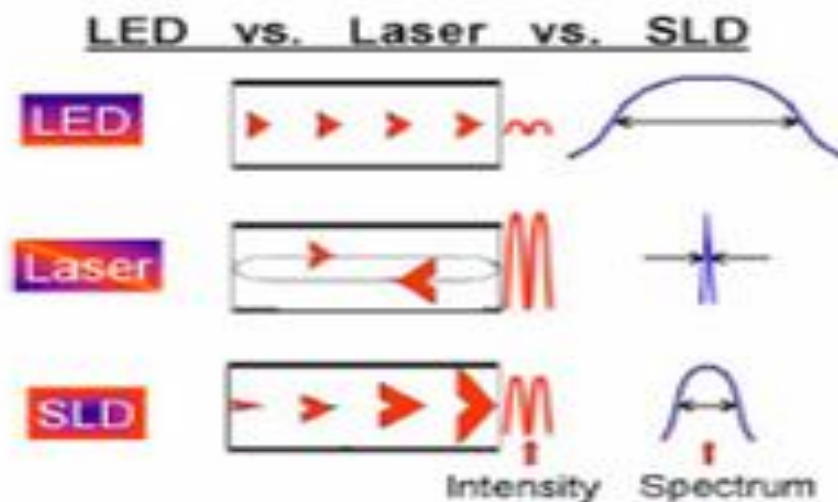


Figure 20: Comparison of LEDs, lasers and SLDs. From [21]

The bandwidth of an optical source relates to its coherence: the wider the bandwidth, the shorter the coherence length and the less coherent the light source. For any coherent light source, speckle noise can limit the SNR of the optical measurement. Piao and Pogue⁷¹ performed experiments and showed that the SNR using a broadband, incoherent light source (eg Led or white lamp with NIR long-pass filter), was much better than earlier measurements with a SLD. It has also been shown that modulation of LEDs reduces noise due to ambient light from, for example, daylight, room lights or computer monitors⁵².

To carry the light to and from the head, optical fibers are usually used. Those used for the sources can be small (.4mm diameter) while those for the detectors should be large (3mm diameter) to collect more light from the head³. Haensse et al.⁷² have even built LEDs directly on sensors, thereby circumventing the problem of sending the light between them.

To collect the light after it has reemerged from the tissue detectors have to be used. The most common detectors are photomultipliers (PMTs) and Avalanche Photo-diodes (APDs). Both types operate in current mode or photon counting mode²⁵. Photon-counting methods can provide signals with low noise, although in some cases response times limit their application. Current-based detectors require brighter sources to achieve similarly good statistics. PMTs generally have lower dark currents, higher sensitivity and lower quantum efficiency than APDs. Practically, integrated APDs with protection, amplification and bias electronics are more robust and simplify the implementation of a continuous wave system. The photon-counting methods require small and cheap components.

Another type of detector is the synchroscan streak camera, which in principle allows intensity to be detected at different points on the tissue through the use of separate optical fibers. Advantages include speed and flexibility, but it is large and expensive and has limited dynamic range².

6.2: Optode Placement

Amita et al.⁴¹ developed a flexible adjustable surface holder (FLASH) to help keep distance between source and detector constant, while adjusting for different size heads. The basic structure consists of sides and nodes making up triangles and quadrangles. Optode sockets are located on the nodes. The material of the sides is flexible, not stretchable. The sum of the interior angles can be changed by allowing deflection of the sides and their rotation at the socket positions. Thus, FLASH is able to change size and shape without changing the source-detector distance.

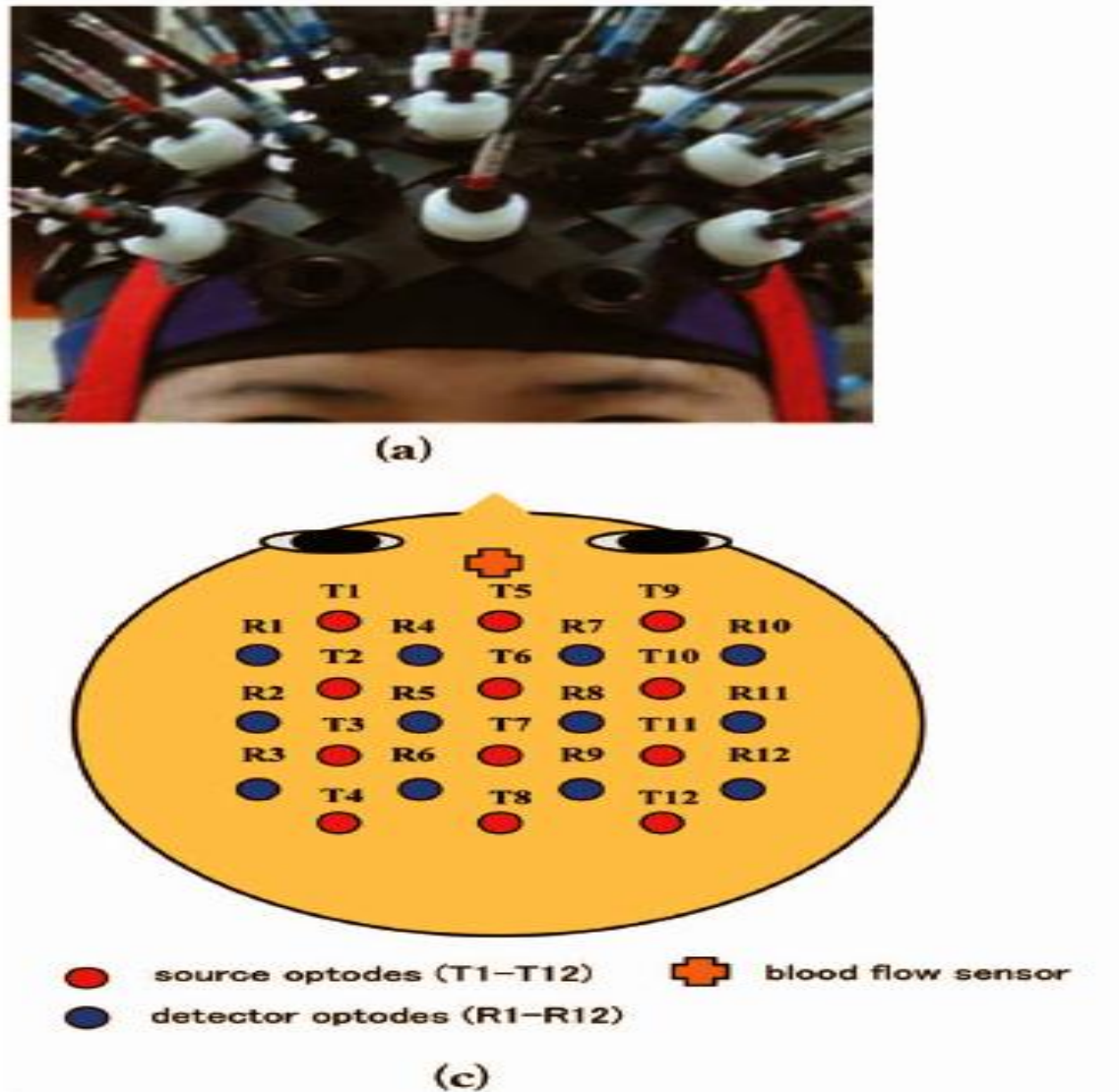


Figure 21: FLASH. From [41]

The arrangement of the sources and detectors on this cap deserves mention. Suppose there are only one source and one detector. Then consider the effect of a small particle inside the head along the path traversed by the photons. Gratton et al⁶⁴ have shown that the fast optical signal in this case is most sensitive to particles directly under the source and detector, and not very sensitive to the region in between. Now if we consider two sources and two detectors, arranged perpendicularly, and examine the effect of a particle on the light path, we see that the region where the signals are most affected moves

closer to the mid-point and deeper in the tissue. The effect of adding two more source-detector pairs is shown below.

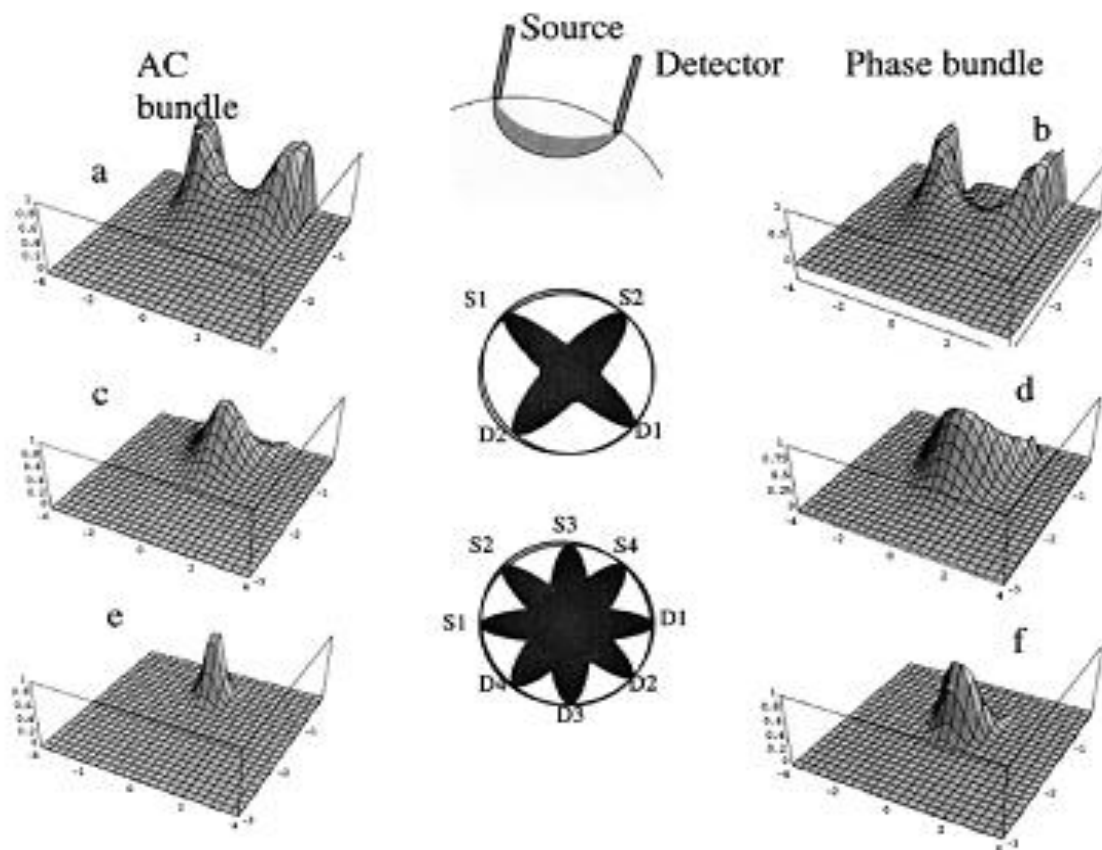


Figure 22: Pi detector. From [64]

So, arranging multiple sources and detectors as shown increases the depth of interrogation. The 4 source-detector pair arrangement is called a Pi detector.

6.3: Encoding Schemes

NIR tomography measurement of discriminated S-D signals can be described intuitively by the following matrix equation: $\underline{\underline{M}}_{N \times 1} = \underline{\underline{\Gamma}}^{-1}_{N \times N} \underline{\underline{W}}_{N \times N} \underline{\underline{\Gamma}}_{N \times N} \underline{\underline{S}}_{N \times 1}$, where $\underline{\underline{S}}$ denotes the source, $\underline{\underline{\Gamma}}$ the encoding, and $\underline{\underline{W}}$ the sensitivity matrix determined by the optical properties of the medium, as well as the geometry of the imaging array⁷¹. When the source encoding is performed by sequential switching, we must

include a time dependence in the encoding matrix. This is the most straightforward encoding but is limited in speed. Frequency multiplexing requires a frequency dependence of the encoding. Although the S-D pairs can be sampled simultaneously, the dynamic range is linearly reduced when adding more sources. A more robust method of encoding is the spectral-encoding technique. Multiple LDs are used in this configuration, and the encoding matrix has wavelength dependence. Then we can write out the matrix equations as follows:

$$\begin{bmatrix} M_1 \\ M_2 \\ \vdots \\ M_N \end{bmatrix} = \begin{bmatrix} 1/\langle \lambda_1 \rangle & & & \\ & 1/\langle \lambda_2 \rangle & & \\ & & \ddots & \\ & & & 1/\langle \lambda_N \rangle \end{bmatrix} \begin{bmatrix} W_{11} & & & \\ & W_{22} & & \\ & & \ddots & \\ & & & W_{NN} \end{bmatrix} \begin{bmatrix} \langle \lambda_1 \rangle \\ \langle \lambda_2 \rangle \\ \vdots \\ \langle \lambda_N \rangle \end{bmatrix} \begin{bmatrix} S_1 \\ S_2 \\ \vdots \\ S_N \end{bmatrix} \quad (41)$$

This performs all decoding prior to photoelectric conversion, thereby allowing for a higher sampling speed without compromising the dynamic range of each channel.

Using a low coherence source, we can reduce the spontaneous channel-to-channel intensity fluctuations. The system is shown next:

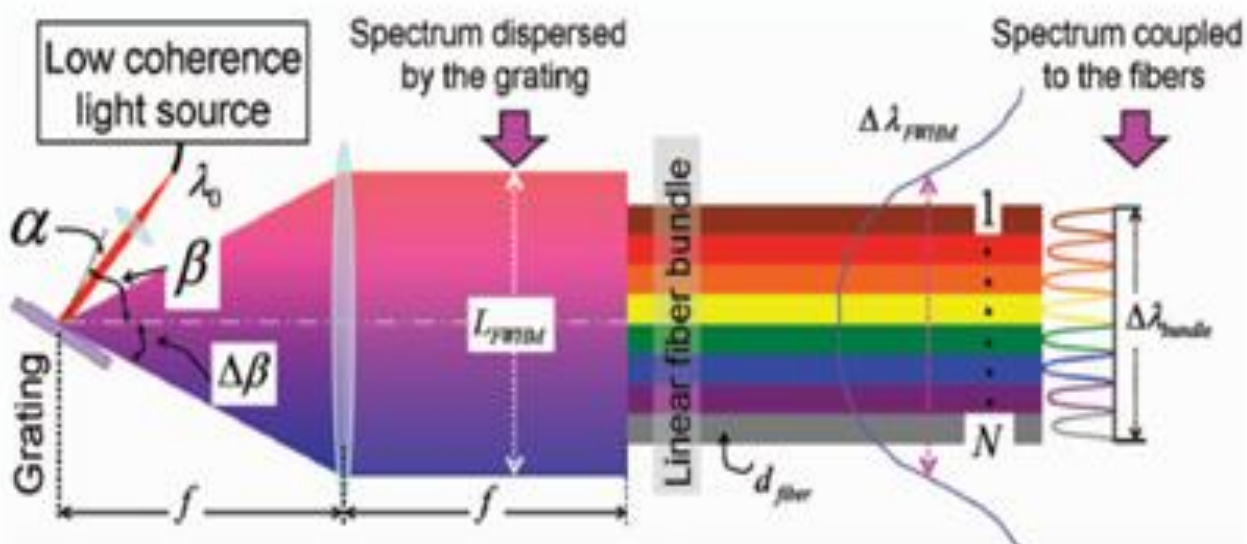


Figure 23: Low-coherence wavelength encoding. From [71]

In this case, the wavelengths in the previous equation can be replaced as follows:

$$\langle \lambda_n \rangle = \left\langle \lambda_0 + \left(n - \frac{N+1}{2} \right) \Delta \lambda_{Fiber} \right\rangle \quad (42)$$

where N is the total number of fibers and is even, λ_0 is the center wavelength of the overall spectral band coupled to the fiber bundle and $\Delta \lambda_{Fiber}$ is the bandwidth coupled to each fiber.

6.4: Spectroscopy Systems

6.4.1: Continuous Wave

Continuous wave systems are conceptually the simplest type and cheapest of the NIR spectroscopy systems. They emit a constant intensity source, and detect intensity continuously. Thus, measurements of attenuation changes can be made. Using a value for the differential path length factor from the literature, calculation of chromophore concentration changes is possible via the modified Beer-Lambert Law.

6.4.2: Time-Resolved

In time-resolved spectroscopy (TRS), a short light pulse (2-5ps) is delivered to the sample at a time t_0 . The scattering effects of the tissue give rise to a temporal point spread function in intensity²¹. The time \bar{t} , which should be wavelength dependent, at which the maximum intensity occurs relative to the input pulse is the mean arrival time of the photons, and this can be used to compute the mean optical path length, which can be used in the modified BLL as the optical path length. Specifically, we have

$$\bar{L} \cdot \zeta(\lambda) = \frac{c_v}{n} \bar{t}(\lambda) \quad (43)$$

where c_v is the speed of light and n is the refractive index in the tissue. Now, if we use the second form of the BLL we then can calculate the attenuation due to absorption and scattering as

$$A(\lambda) = \ln(I(\lambda)/I_0(\lambda)) = (\mu_a(\lambda) + \mu_s(\lambda)) \cdot \bar{L} \cdot \zeta(\lambda) = (\mu_a(\lambda) + \mu_s(\lambda)) \cdot \frac{c_v}{n} \bar{t}(\lambda) \quad (44)$$

Note, however, that using the optical path length as determined by time-resolved measurements induces errors in the concentration calculations because the partial path length in the brain is significantly shorter than the calculated optical path length, an error known as the partial volume effect⁷³. Some disadvantages of TRS include a high level of noise, physical size of the instrumentation and its cost²⁷.

6.4.3: Frequency Domain

In frequency-domain spectroscopy (FDS), a constant source is intensity modulated and detected beam exhibits a phase shift due to propagation delay, absorption and scattering. The detected intensity is of the form

$$I(\lambda) = I_{dc}(\lambda) + I_{ac}(\lambda) \cdot \sin(2\pi\nu \cdot t - \phi(\lambda)) \quad (45)$$

Since these instruments induce a phase delay, they are sometimes referred to as delay instruments. The phase measurement allows for calculation of optical path length as follows:

$$L \cdot \zeta(\lambda) = \frac{\phi(\lambda) \cdot c_v}{2\pi\nu \cdot n} \quad (46)$$

FDS requires scanning through all radio frequencies. The result is a FT of the time point spread function of TRS. Most of the instruments are single frequency instruments and use a multidistance configuration. From a clinical point of view, the advantages are represented by easier transportability and commercial availability²⁷.

Two modulation schemes are currently used to extract information from the detector of an FD system. Homodyne systems use in-phase and quadrature demodulation circuits to measure the phase and amplitude of the signal, while heterodyne systems mix the signal with a reference, yielding a low-frequency sine wave that has the same phase and amplitude as the original signal⁵⁷.

In a heterodyne system, the light source is modulated at RF, and measurement is made of intensity, phase shift and modulation depth. Detection of small changes in phase or modulation depth is difficult, so almost all instruments employ some down conversion into audio frequencies where

conventional phase detection techniques can be applied. One way to do this demodulation with PMTs is to modulate the detector gain at a frequency a few kHz from the light source modulation frequency resulting in direct demodulation in the detector. The detector output is then an AF signal at the difference frequency². This allows for the use of relatively inexpensive ADCs⁷⁴.

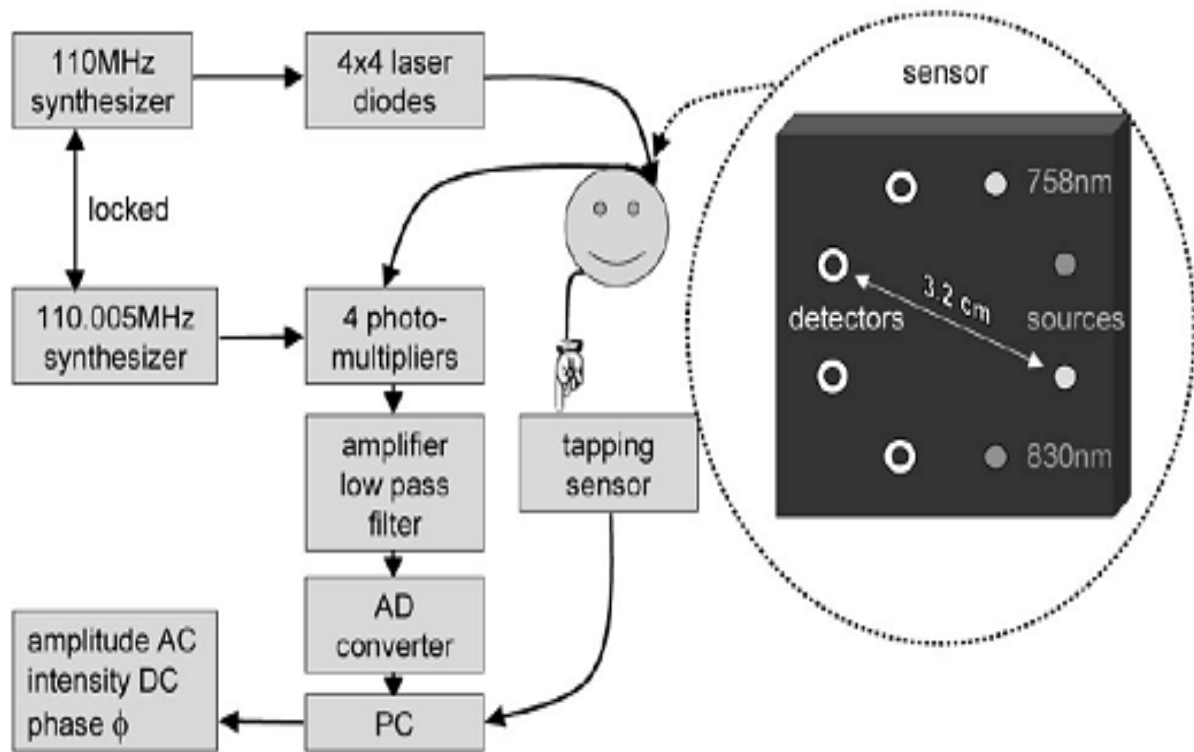


Figure 24: Heterodyne system. From [47]

Homodyne systems work as follows. A standard in-phase and quadrature (I&Q) demodulator gives an I&Q signal within its working frequency range ω and detects the amplitude and phase of a desired sinusoidal signal⁷⁵. The signal under test has the form $2A\sin(\omega t + \theta)$. The system is shown below:

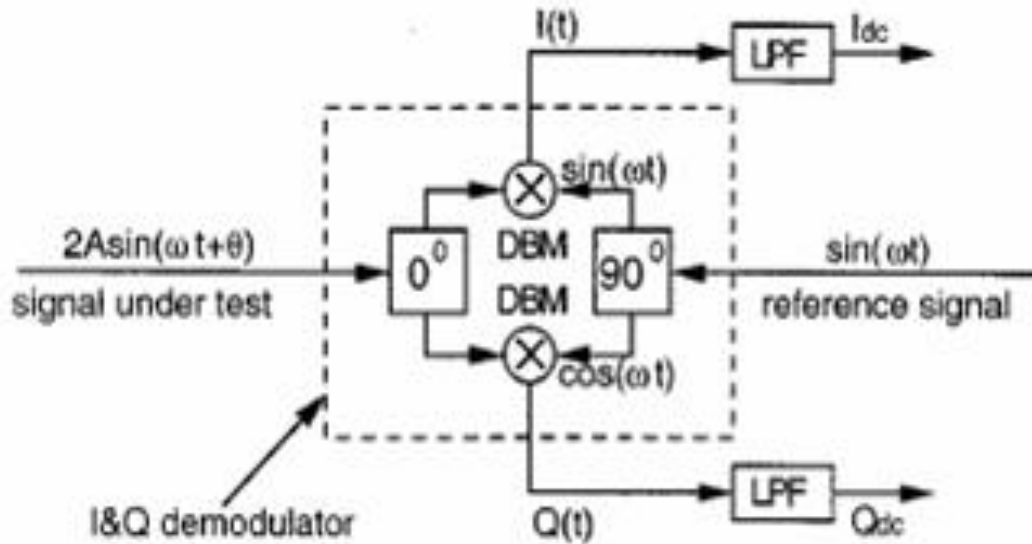


Figure 25: I&Q demodulator. From [75]

One of the double-balanced mixers produces an output:

$$I(t) = 2A \sin(\omega t + \theta) \sin(\omega t) = A \cos(\theta) - A \cos(2\omega t + \theta) \quad (47)$$

And the other

$$Q(t) = 2A \sin(\omega t + \theta) \cos(\omega t) = A \sin(\theta) + A \sin(2\omega t + \theta) \quad (48)$$

Note that the high frequency components can be eliminated by use of an LPF, and the phase and amplitude of the desired signal can be found as

$$\theta = \tan^{-1} \left(\frac{Q_{DC}}{I_{DC}} \right) \quad (49)$$

$$A = \left(I_{DC}^2 + Q_{DC}^2 \right)^{1/2}$$

For frequency-division multiplexing, the following system is used:

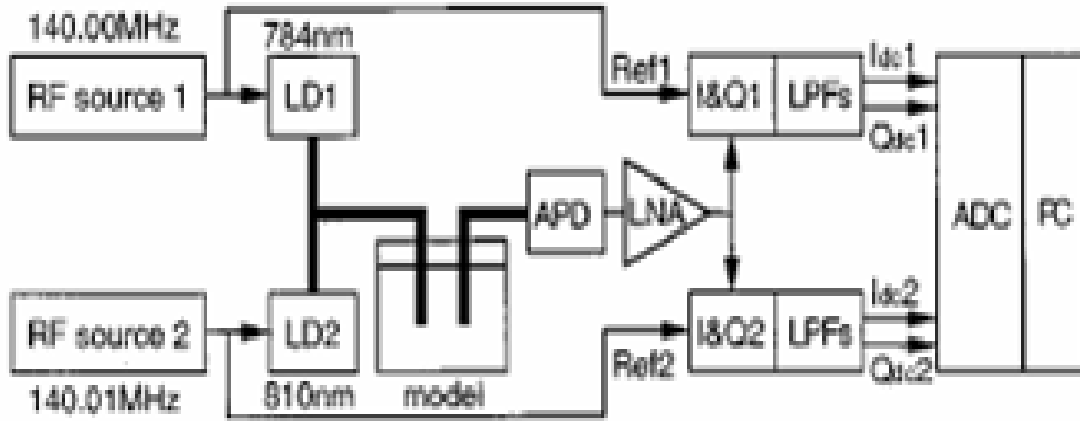


Figure 26: Frequency-division multiplexing system. From 75

The functioning relies on the premise that $\omega_2 - \omega_1 = \Delta\omega \ll \omega_1$. Note that the line connecting the two LDs consists of an adder. Then, the output of I&Q1 is

$$\begin{aligned} I(t) &= A_1 \cos(\theta_1) - A_1 \cos(2\omega_1 t + \theta_1) + A_2 \cos[(\omega_1 - \omega_2)t + \theta_2] - A_2 \cos[(\omega_1 + \omega_2)t + \theta_2] \\ Q(t) &= A_1 \sin(\theta_1) - A_1 \sin(2\omega_1 t + \theta_1) + A_2 \sin[(\omega_1 - \omega_2)t + \theta_2] - A_2 \sin[(\omega_1 + \omega_2)t + \theta_2] \end{aligned} \quad (50)$$

By applying proper low-pass filters to each branch, we can extract the phase and amplitude values.

6.4.4: Comparison

In a heterogeneous surface-bound media, delay and intensity measures are sensitive to both absorption and scattering changes, although in a different manner. Intensity measures are conceptually simpler. Delay measures are more complex because they occur on the order of picoseconds and require a modulated light source¹⁴. However, delay measures may be particularly sensitive to effects occurring in the brain because changes in brain transparency selectively affect long photon paths. Intensity measures, in contrast, are very sensitive to phenomena, such as capillary and arterial pulsation, occurring superficially and thus influencing all photons in a similar manner⁷⁷. Intensity measurements are also more sensitive to superficial and hemodynamic effects than time-of-flight measurements⁷⁶. Additionally, delay measures have better spatial resolution than intensity measures¹⁴.

Since FD instruments contain the same information as TR instruments, all of the above advantages of FD over continuous instruments apply to TR instruments as well. However, in practice, FD instruments have a higher SNR and are faster than TR instruments⁶⁴. In multi-wavelength systems, they are also faster since they do not require switching the sources.

6.5: Examples

A complete list of the main commercially available NIR clinical instrumentation is given in reference [27]. Below are some examples.

Name/Type	Measurement
FD-Oximeter Imagent	Computes phase from Fourier transformed data ⁷⁸
INVOS3100 Somanetics	Measures ratio of light absorption by chromophores ¹
OTIS Archinoetics	CW fNIR that allows sensing over hair ⁷⁹
OMM300 Shimadzu	Utilizes FLASH. Remote control capable ⁸⁰
OMNIA ISS Inc.	Phase and intensity measurements ⁴⁹
Custom Made	Time-resolved optical imager for assessment of cerebral oxygenation

CHAPTER 7: FAST SIGNAL EXPERIMENTAL RESULTS

This chapter is a very brief summary of some experimental results related to the fast signal.

Harper et al.⁸³ assessed relationships of evoked electrical and light scattering changes from cat dorsal hippocampus following Schaeffer collateral stimulation. Stimuli elicited a complex synaptic potential that lasted 100-200ms depending on stimulus intensity and electrode position. Light scattering changes peaked 20ms after stimuli and occurred simultaneously with population spikes. A long-lasting light scattering component peaked 100-500ms after the stimulus, concurrently with larger population postsynaptic potentials. The peak of the fast response first increased and then decreased with increasing stimulation current, indicating that inhibitory mechanisms may be recruited at higher stimulus intensities.

McCluskey et al.⁵⁶ made measurements to test the ability of a heterodyne system to measure optical changes in an isolated nerve, under conditions in which diffusion is not achieved, and phase changes could only be due to scattering effects. The experiments indicate that the phase change of modulated light (110 MHz) in lobster nerved due to changes in scattering is less than $.01^\circ$.

Gratton et al.³¹ experimented in visual, auditory, somatosensory and motor cortices. All studies showed EROS response of a similar nature: increases in photon delay of a few picoseconds, simultaneous with concurrently recorded evoked potentials, and when measured, co-localized with the BOLD fMRI responses. Gratton et al.⁸² also tested and confirmed the ability of EROS to demonstrate sequential activation of neighboring cortical areas, such as the early visual areas in the occipital cortex. Stimuli consisted of black-and-white checkerboards alternating at different frequencies (1,2,4,6 and 8Hz). Finally, Gratton et al.⁷⁸ show how EROS can identify two adjacent, but distinct, areas in the superior/middle temporal cortices (S/MTC) that are involved in the processing of semantic and syntactic anomalies and are associated with scalp-recorded electrical activity.

CHAPTER 8: OTHER OPTICAL METHODS

8.1: Optical Coherence Tomography

Optical Coherence Tomography (OCT) is a high-resolution, depth-resolved imaging method. It overcomes problems of scattering by using coherence to isolate light that has been directly backscattered⁸⁴. This light has the shortest path through the tissue.

OCT is based on an interferometer consisting of a low-coherence light source with a broad spectral width, a detector and a beam splitter, as well as sample and reference arms. A scanner placed in the reference arm changes the arm's length, allowing photons backscattered from the sample to be collected at different depths. The detection of the backscattered photons is based on observing interference between photons coming from the sample and reference arms. To form interference, the path length difference of these photons must be smaller than the coherence length of the light source⁸⁵.

8.2: Imaging with Voltage-Sensitive Dyes

Optical imaging with voltage-sensitive dyes permits the visualization of cortical activity with a sub-millisecond time resolution and a spatial resolution of 50-100 microns⁸⁶. The preparation under study is first stained by bath application of the dye. The dye molecules bind to the external surface of excitable membranes and act as molecular transducers that transform changes in membrane potential into optical signals. The resulting changes in absorption of emitted fluorescence occur in microseconds and linearly correlate with the electrical activity of stained neurons. A variety of voltage-sensitive dyes or ion-selective indicators have been developed to allow optical imaging of dynamic neural activation. However, the photo-toxicity of the dyes and the difficulty of the loading procedures limit their application¹⁰⁶.

8.3: Optical Probes

By functionalizing probes to specific cellular and molecular sites, the detection and spatial localization of the probes through imaging techniques add molecular specificity⁸⁷. Advancement of highly sensitive detection systems and cooled CCD cameras has permitted detection of extremely weak fluorescent and bioluminescent signals originating deep within highly scattering tissue. Probe types include scattering probes, modulating probes and absorption probes, the simplest of which are NIR dyes.

8.4: Optical Phase Conjugation

Elastic optical scattering is a deterministic and time-reversible process. If we can record the phase and amplitude of a propagating light field completely and reproduce a back-propagating phase-conjugated (or time-reversed) field, this field should be able to retrace its trajectory through the scattering medium and return the original input light field⁸⁸.

Yaqoob et al.⁸⁸ examined whether phase conjugation, through animal tissue, was feasible. In the study, the target was a .46mm thick chicken breast tissue. Light at 532nm with a $1/e^2$ beam size was shone. The schematic looks as follows:

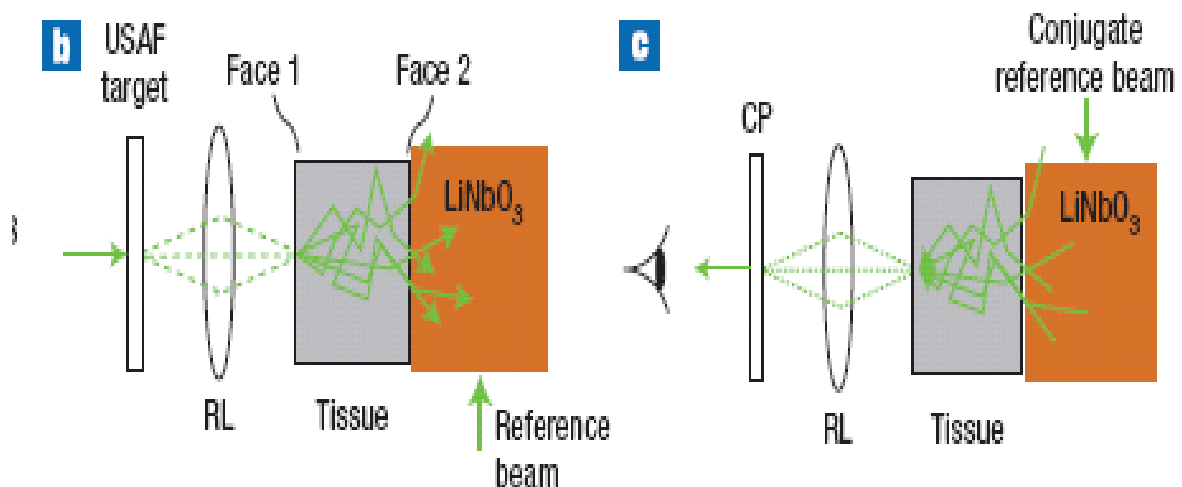


Figure 27: Schematic for optical phase conjugate recording. From [88]

The rightmost component is usually called a phase conjugate mirror and must be capable of holographic recording. Mathematically, the interaction of the incident field with a scattering medium can be expressed as:

$$\begin{bmatrix} b_1 \\ b_2 \end{bmatrix} = \begin{bmatrix} \bar{S}_{11} & \bar{S}_{12} \\ \bar{S}_{21} & \bar{S}_{22} \end{bmatrix} \begin{bmatrix} a_1 \\ a_2 \end{bmatrix} \quad (52)$$

where the S matrix is associated with the medium and the a vector is the input light field.

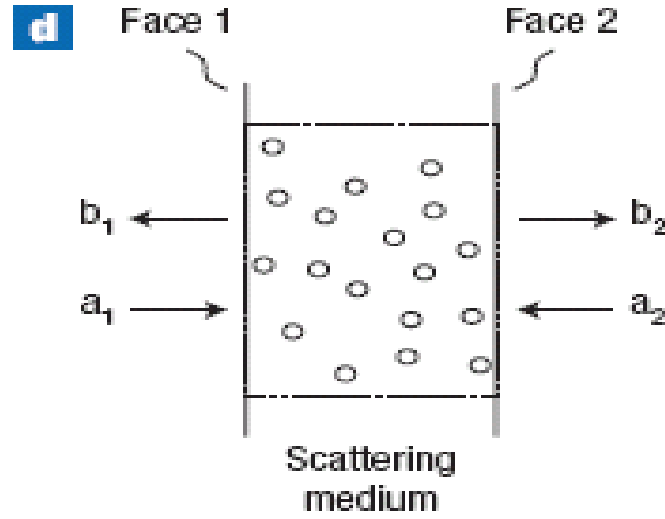


Figure 28: Physical situation for phase conjugation. From [88]

We also set $a_2 = 0$. In this case, the light field impinging on the PCM is $b_2 = \bar{S}_{21}a_1$. Then, the OPC light field travelling back towards face 2 can be expressed as $\psi_{PC} = \bar{A}\bar{S}_{21}^*a_1^*$ where \bar{A} represents the reduction in angular range of the reconstructed wave owing to the incomplete recording and playback of the transmitted wave. The reconstructed light field on face 1 can be written as $\psi_{REC} = \bar{S}_{12}\bar{A}\bar{S}_{21}^*a_1^*$. In the ideal case, the capture of the initial light transmission is complete and therefore \bar{A} is unitary. Also, the medium is lossless and backscattering is absent, which, by energy conservation, leads to $\bar{S}_{12}\bar{S}_{12}^H = I$, so that we can write $\psi_{ID,REC} = a_1^*$.

In each experiment, the transmitted light through the tissue was first holographically recorded in the crystal for 30s. Next, a conjugate reference beam is used to generate the OPC light field which travelled back through the tissue. They displaced the tissue laterally in incremental steps as well. That displacement and its effects are illustrated in the figure below.

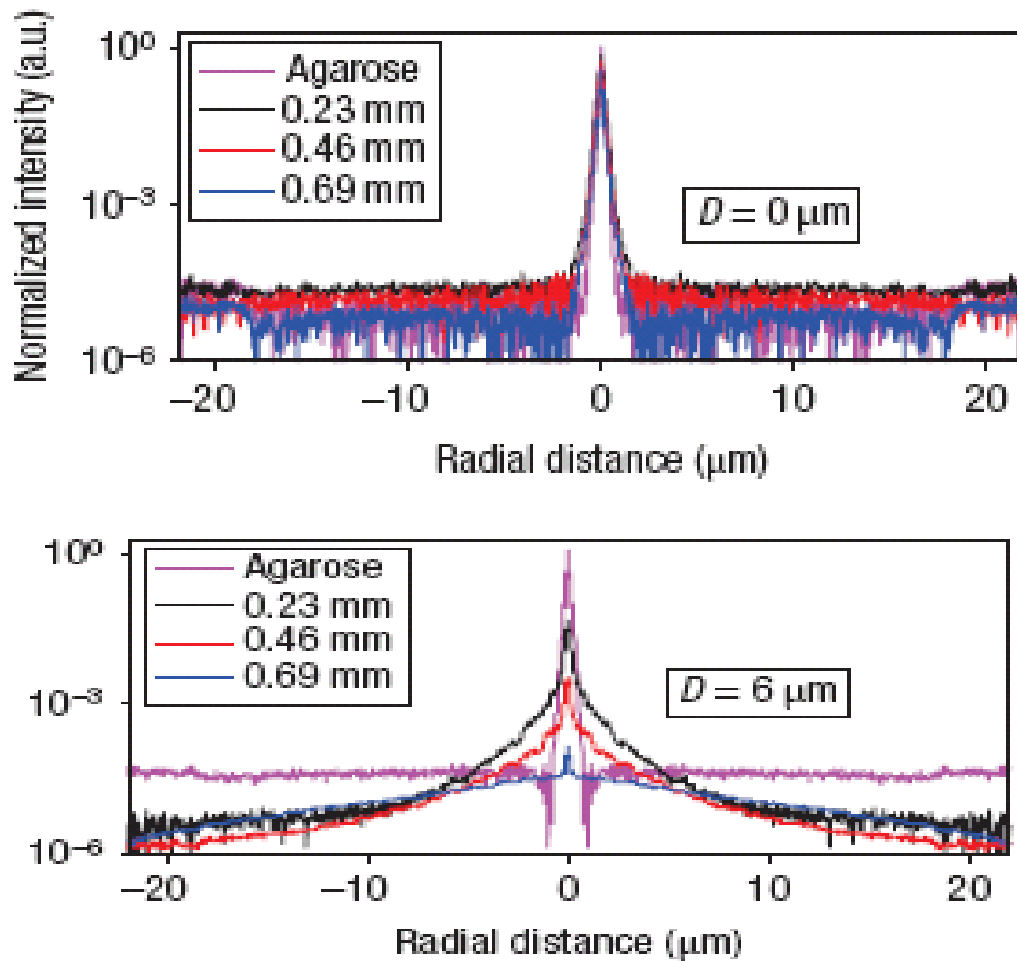


Figure 28: Intensity of phase conjugate reconstructed light field. From [88]

8.5: Other Methods

A description of a number of other methods, including Laminar OT and diffuse optical imaging can be found in reference [84].

CHAPTER 9: BRAIN COMPUTER INTERFACES (BCIS)

9.1: Introduction

‘A brain-computer interface is a communication system that does not depend on the brain’s normal output pathways of peripheral nerves and muscles’⁸⁹. All other augmentative communication technologies require some form of muscle control. Each BCI uses a particular algorithm to translate its input into output control signals. This algorithm might include linear or nonlinear equations, a neural network, or other methods, and might incorporate continual adaptation of important parameters to key aspects of the input provided by the user.

At the highest level, BCI designers are faced with the modeling problem: what level of physiological detail and physical insight should be used to design a brain computer interface? Designers choose between three approaches: white box, gray box or black box.⁹¹ The white box would require the highest level of physiological detail. Model implementation would require the parameterization of the complete motor system. In the gray-box approach, one could take a particularly important feature of the nervous system, incorporate this into the model and then use data to determine the rest of the unknown parameters. In the black box case, it is assumed that no physical insight is available for the model. Wiener filters and neural networks are useful for the black box approach. In practice, the type of modeling is dictated by the application of the BCI system.

BCI technology may have something to offer in terms of physical recovery for certain conditions through reinforcement of damaged neural pathways, plasticity-induced reorganization and triggering of functional electrical stimulation⁹⁰. For example, a motor imagery system, coupled to an implanted neuroprosthesis system, has been used to help a paralyzed patient¹⁷. BCIs can also help in situations where verbal communication is difficult, for example, during military operations. The applications of BCI systems are vast, although there are a number of technical difficulties involved when designing

BCIs. Overcoming difficulties like low information transfer rates and difficulty in signal detection will pave the way for a new type of communication system, one which does not rely on the normal output pathways of the brain.

Mason et al.⁹² provides a comprehensive review of BCI technology.

9.2: Performance

There were 3 BCI competitions, arranged in 2001, 2002 and 2004, respectively⁹⁴. The first competition was a test to see how such an enterprise would work and how much attention it would attract. In the second competitions, they provided a broad range of typical BCL problems. For the third competition, they provided analysis challenges that are relevant to present BCI research.

Even with the widespread attention that BCI has been getting over the past 15 years, there are few performance metrics for BCIs and therefore comparisons between methods and systems are difficult. One metric that has been chosen to measure performance of BCIs is the information transfer rate, measure in bits per minute⁹³:

$$ITR = \frac{\#decisions}{total_duration} \cdot \left(p \log_2 p + (1-p) \log_2 \left(\frac{1-p}{N-1} \right) + \log_2 N \right) \quad (53)$$

where p is the accuracy of the subject in making decisions between N targets.

Sambasivan and Jackson¹⁰⁰ address how to design BCIs taking into account everyday activity and values of the patient. Some chosen metrics with which to evaluate system performance include visibility of status (ie, feedback within reasonable time), user freedom, flexibility and efficiency. Furthermore, the BCI should be context-aware, for example, when a person approaches the user, a speech application could open.

Future research in the area of performance metric selection should result in generation and selection of more suitable cost functions that guide the model search procedure more efficiently⁹⁵, and help to make the design of efficient BCIs feasible.

9.3: Optical BCIs

Some examples of optical BCIs are given in this section. All of these BCIs are based on the slow optical signal since it is more reliable than the fast optical signal. Also, appropriate features are more easily found and tested using the slow signal. Future research should examine possible features of the fast signal that can be extracted and used for classification purposes. Since the slow optical signal occurs on the order of seconds, real-time responses of these optical BCIs are impractical. However, with the addition of fast signals to BCI signal acquisition, it is possible that faster and more efficient BCIs can be developed.

Gratton et al.³³ developed a NIRS-BCI. Its system architecture is shown below.

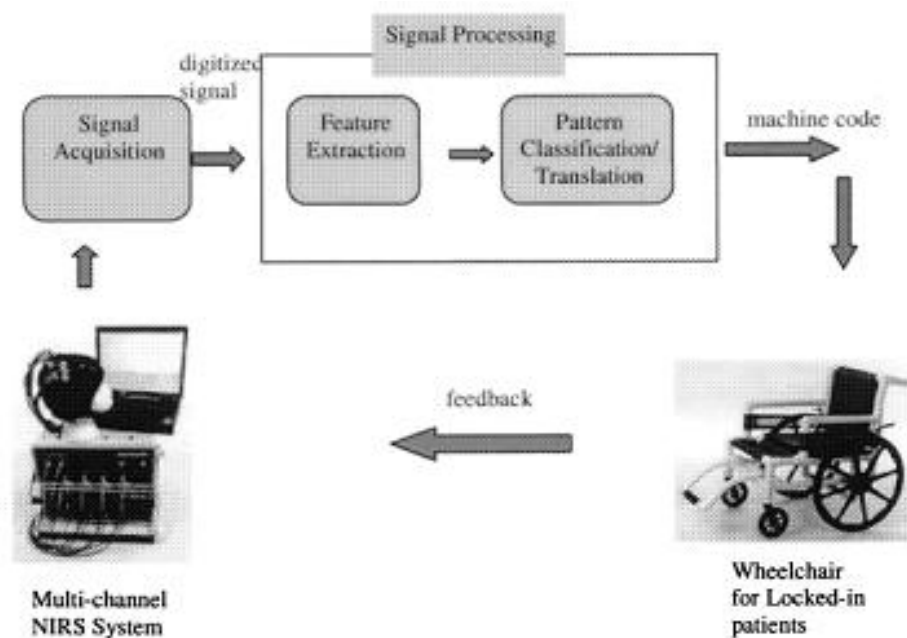


Figure 30: Architecture for NIRS-BCI. From [33]

Note that the wheelchair can be replaced by a neuroprosthetic device.

Coyle et al.⁹⁸ also developed an optical BCI using NIR illumination. Physiological noise, namely the cardiac cycle, respiratory effects and the Mayer wave, are the greatest noise sources inherent in the system. The Mayer wave in particular can lead to feature classification errors as it can be of similar time-course and amplitude as the event-related response. Coyle et al.⁹⁹ also designed an NIRS-BCI that requires little user training. The average oxy-haemoglobin concentration level is calculated every second and a 20-second window of data is analyzed. An event is noted if the average oxy-haemoglobin concentration is greater than a reference level. The reference is set to the maximum level occurring during the first ten seconds of the window. The system has an information transfer rate of 3 bpm.

One final example of an optical BCI was developed by Utsugi et al.⁹⁶. The flow of the signal processing looks like:

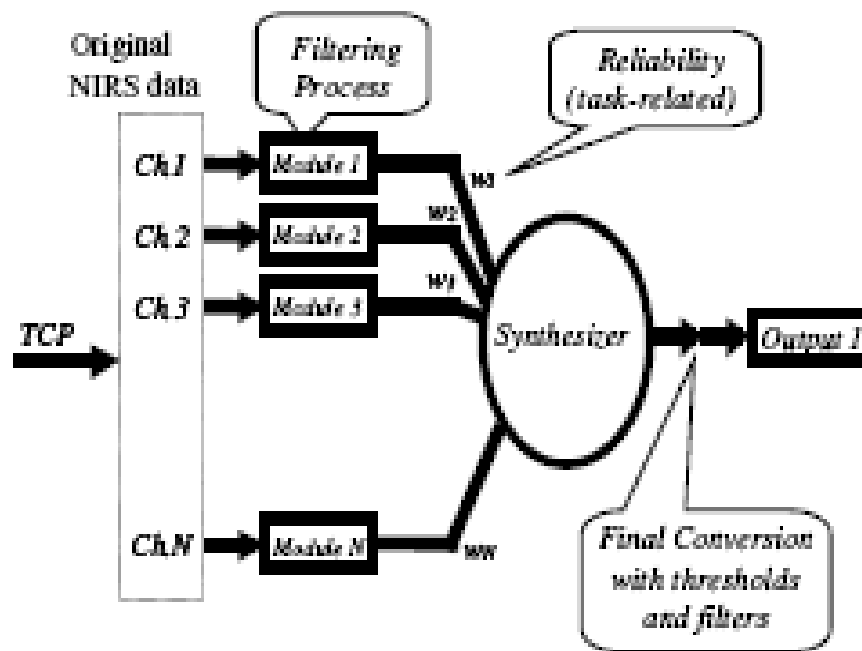


Figure 31: Signal Processing flow for optical BCI. From [96]

The synthesizer calculates a linear combination of module outputs, $s_i(t)$, by using a reliability weight w_i , where i indicates the module id. The RW is a personal, task-related parameter that is

determined by intensity and that is repeatedly evaluated in calibration mode. Finally, adaptive thresholds and filtering are applied to this linearly combined output. A threshold process y is determined by optimizing this value based on the calibration test.

9.4: Other BCIs

There are more BCIs based on electrical brain signals than there are based on optical signals. BCIs have been designed using the SCP, sensorimotor rhythm, and the P300, all component of EEG¹⁰¹. For the sensorimotor rhythm, it has been reported that healthy subjects and paralyzed patients achieve voluntary control of left and right SMRs by imagining movements.

Most EEG-BCIs rely upon the user's ability to learn to modulate the amplitude of a specific EEG frequency band at one or more electrode locations, while others take advantage of evoked potentials, the non-voluntary synchronous cortical responses to an external stimulus¹⁵. Some systems allow subjects to control a computer cursor or other devices by modulating ongoing slow cortical potentials, mu- or beta rhythm amplitudes. These systems have provided a communication platform for persons with advanced ALS. However, EEG-BCIs have several limitations, including 1) the need for extensive training, 2) considerable setup time for each session 3) the implied requirement for focused attention, 4) limited information transfer rates and 5) limited spatial resolution.

Birbaumer and Cohen¹⁰² developed an invasive BCI uses subdural macro-electrodes that are implanted over frontal regions. For this BCI, patients attempted spelling or performed motor imagery tasks. In a single session with these patients, it was possible to differentiate imagination of hand, tongue and mouth movements using ECoG. Support vector machines were used as classification algorithms.

Müller et al.¹⁰³ discusses the Berlin Brain Computer Interface is a non-invasive, EEG- based system whose key features are 1) the use of motor imagery for control tasks and 2) advanced machine learning techniques that automatically extract complex high-dimensional features and classify in a robust manner

and, as a consequence, 3) no need for subject training. The BBCI system needs only 7-20min of calibration. The BBCI has mainly studied two paradigms: (a) the discriminability of pre-movement potentials in self-paced executed movements, where it can be shown that high information transfer rates from single-trial classification of fast-paced motor commands and (b) motor imagery. Some applications of the BBCI include text entry with Hex-o-Spell and monitoring of mental states.

Only limited clinical data are available on BCI use by those with severe neuromuscular disabilities⁸⁹. The Thought Translation Device, which uses SCPs, and the Wadsworth BCI, which uses mu and beta rhythms, have been evaluated in small numbers of users with amyotrophic lateral sclerosis, stroke, spinal cord injury, cerebral palsy or amputation.

.There are also a few BCIs based on magnetic resonance. Yoo et al.¹⁰⁴ Implemented a fMRI-BCI and designed it to detect the different spatial patterns of brain activities generated from four different covert functional tasks performed by the subjects. The temporal resolution is marginal (2-min for command generation). The tasks were simple mental calculation, covert speech generation and motor imagery for either the left or right hand. Another fMRI-BCI was designed by Weiskopf et al.¹⁰⁵. Although fMRI has very good spatial resolution, fMRI-BCIs are severely limited by the slow nature of the response. Also, fMRI-BCIs are highly sensitive to motion artifacts, limiting the portability and repeatability of the systems and experiments with them.

CHAPTER 10: UNEXPLORED RESEARCH QUESTIONS

This chapter focuses on a couple of research questions that have yet to be explored. Firstly, there is the question of how to use the slow optical signal data to help with recognition of fast signals. For example, is there a way to use the fact that an activation of the slow signal occurs to help detect whether the fast signal occurs. Along the same line of thought, possible features for the detection and classification of fast signals has yet to be examined in detail. It would also be useful to relate the features chosen for classification of the slow signal to possible features of the fast signal.

Another area of research related to optical methods is exploration of the optical phase conjugation technique and its applicability to human brain tissue. Specifically, Yaqoob et al.⁸⁸ has shown that it is possible to use phase conjugation methods to reconstruct light fields that are incident on a tissue sample. However, the tissues used in their experiments were much thinner than human brain tissues. Examination of the feasibility of applying these techniques to human brain tissues may prove to be a monumental step in recording fast optical changes in brain properties.

All of the current optical techniques mentioned in this paper use both deterministic and simple methods for tissue illumination. One unexplored research question is how can we vary the input light pattern in order to extract otherwise hidden patterns in the optical changes? If the intensity of the incident light randomly fluctuates, is it possible to observe different dynamic optical changes in the brain? Although theory in this area has yet to be developed, it is possible that experimental work could lead to new directions and new ideas about how the optical properties of the brain change.

Another research question that has yet to be explored is how we can best combine recording modalities to meet the needs of specific applications. Although many experimenters have combined EEG and NIRS, and also fMRI and NIRS, all did so to verify the changes in optical properties based on the data from other modalities. However, none of the researchers examined how to exploit data from one

recording modality in order to better understand the data from another modality. Research in this area may bring about the most profound changes in the way brain data is recorded and interpreted, and could open the door for practical and fast BCIs that can be used at the bedside of every day patients.

REFERENCES

- [1] Owen-Reece, Smith, Elwell and Goldstone. "Near Infrared Spectroscopy". *British Journal of Anaesthesia*, 82(3), pp. 418-26 (1999)
- [2] Delpy and Cope. "Quantification in Tissue Near-Infrared Spectroscopy". *Philos. Trans. R. Soc. Lond. B: Biol. Sci.* 352, pp. 649-59 (1997)
- [3] Gratton and Fabiani. "In Vivo Optical Imaging of Brain Function". In R. Parasuraman and M. Rizzo (Eds.) *Neuroergonomics: The Brain at Work*, pp. 65-81, CRC Press (2002)
- [4] Villringer and Change. "Non-Invasive Optical Spectroscopy and Imaging of Human Brain Function". *Trends in Neuroscience*, Vol. 20, No. 10, pp. 435-442 (1997)
- [5] Gratton and Fabiani. "The Event-Related Optical Signal: A New Tool for Studying Brain Function". *International Journal of Psychophysiology*, 42, pp. 109-121 (2001)
- [6] Gratton and Fabiani, M. "Dynamic brain imaging: Event-related optical signal (EROS) measures of the time course and localization of cognitive-related activity". *Psychonomic Bulletin & Review*, 5, pp. 535-563 (1998)
- [7] List of Regions in the Human Brain. In *Wikipedia, the free encyclopedia*. Modified 29 July 2008, from http://en.wikipedia.org/wiki/List_of_regions_in_the_human_brain
- [8] Devara. 2005. "Signal Processing for Functional Near-infrared Neuroimaging". Master's Thesis, Drexel University
- [9] Parietal Lobe. In *Wikipedia, the free encyclopedia*. Modified 17 June 2008, from http://en.wikipedia.org/wiki/Parietal_Lobe
- [10] Montes and Shahsavari. 2006. "Classifying of EEG signals recorded during right and left-hand finger movements". Master's Thesis, Chalmers University of Technology
- [11] Delpy, Essenpreis and van der Zee. "Optical Properties of Brain Tissue". In R. R. Alfano and B. Chance (Eds.) *Photon Migration and Imaging in Random Media and Tissues*, pp. 454-465, Proc. SPIE 1888 (1993)
- [12] Gratton and Fabiani. "Shedding light On Brain Function: The Event-Related Optical Signal". *Trends in Cognitive Sciences*. Vol. 5, Issue 8, pp. 357-363 (2001)
- [13] EEG. In *Wikipedia, the free encyclopedia*. Modified 8 August 2008, from <http://en.wikipedia.org/wiki/EEG>
- [14] Gratton and Fabiani. "Fast Optical Signals: Principles, Methods and Experimental Results". In Frostig (Ed.) *In Vivo Optical Imaging of Brain Function*, pp. 224-245, CRC Press (2002)
- [15] Donoghue and Hochberg. "Sensors for Brain-Computer Interfaces". *IEEE Engineering in Medicine and Biology Magazine*, pp. 32-38 (Sept/Oct 2006)
- [16] Bai1, Lin, Vorbach, Floeter, Hattori and Hallett. "A High Performance Sensorimotor Beta Rhythm-Based Brain-Computer Interface Associated with Human Natural Motor Behavior". *J. Neural Eng.* 5, pp. 24-35 (2008)
- [17] Lebedev and Nicolelis. "Brain-Machine Interfaces: Past, Present and Future". *Trends in Neuroscience*, Vol. 29, No. 9, pp. 536-546 (2006)
- [18] ECoG. In *Wikipedia, the free encyclopedia*. Modified 26 July 2008, from <http://en.wikipedia.org/wiki/ECoG>
- [19] MRI. In *Wikipedia, the free encyclopedia*. Modified 12 August 2008, from <http://en.wikipedia.org/wiki/MRI>
- [20] Weiskopf, Mathiak, Bock, Scharnowski, Veit, Grodd, Goebel, and Birbaumer. "Principles of a Brain-Computer Interface (BCI) Based on Real-Time Functional Magnetic Resonance Imaging (fMRI)". *IEEE Transactions on Biomedical Engineering*, Vol. 51, No. 6, (June 2004)

- [21] Rolfe. "In Vivo Near-Infrared Spectroscopy". *Annual Rev. Biomed. Eng.*, Vol. 2, pp. 715-54 (2000)
- [22] Pulse Oximetry. . In *Wikipedia, the free encyclopedia*. Modified 12 August 2008, from http://en.wikipedia.org/wiki/Pulse_oximetry
- [23] Bunce, Izzetoglu, M., Izzetoglu, K, Onaral, Pourrezaei. "Functional Near-Infrared Spectroscopy: An Emerging Neuro-Imaging Modality". *Engineering in Medicine and Biology Magazine, IEEE*, 25(4), pp. 54-62 (July/Aug 2006)
- [24] Hoshi. "Functional Near-Infrared Spectroscopy: Current Status and Future Prospects". *Journal of Biomedical Optics*, 12(6), 062106 (Nov/Dec 2007)
- [25] Matthews, Pearlmutter, Ward, Soraghan, Markham. "Hemodynamics for Brain-Computer Interfaces". *Signal Processing Magazine, IEEE*, 25(1), pp. 87-94 (2008)
- [26] Coyle, Markham and Ward. "An Optical Brain-Computer Interface". *Biomedizinische Technik Proc. 2nd Int. Brain-Computer Interface Workshop and Training Course*, Vol. 49, pp 45-46 (2005)
- [27] Ferrari, Quaresima and Wolf. "Progress of near-infrared spectroscopy and topography for brain and muscle clinical applications". *Journal of Biomedical Optics*, 12(6), 062104 (Nov/Dec 2007)
- [28] Orbig and Villringer. "Beyond the Visible—Imaging the Human Brain with Light". *Journal of Cerebral Blood Flow and Metabolism*, 23, pp. 1-18 (2003)
- [29] Uludag, Kohl, Steinbrink, Obrig, and Villringer. "Cross talk in the Lambert-Beer Calculation for Near-Infrared Wavelengths Estimated by Monte Carlo Simulations". *J. Biomedical Optics*, Vol. 7, No. 1, pp. 51-59 (2002)
- [30] Sato, Kiguchi, Kawaguchi, and Maki. "Practicality of wavelength selection to improve signal-to-noise ratio in near-infrared spectroscopy". *NeuroImage*, Vol. 21, pp. 1554-1562 (2004)
- [31] Gratton, Low, & Fabiani. "Time Course of Executive Processes: Data from the Event-Related Optical Signal". In S. A. Bunge & J. D. Wallis (Eds.), *Perspectives on Rule-Guided Behavior*, pp. 197-223, Oxford University Press (2008)
- [32] Yao and George. "Dynamic neuroimaging of retinal light responses using fast intrinsic optical signals". *NeuroImage* 33, pp. 898-906 (2006)
- [33] Gratton, Brumback, Gordon, Pearson, Low, and Fabiani. "Effects of measurement method, wavelength, and source-detector distance on the fast optical signal". *NeuroImage* 32, pp. 1576-1590 (2006)
- [34] Gratton, Fabiani, Elbert and Rockstroh. "Seeing right through you: Applications of optical imaging to the study of the human brain". *Psychophysiology*, 40, pp. 487-491 (2003)
- [35] Gratton, E., Fantini, Franceschini, Gratton, M. and Fabiani. "Measurements of scattering and absorption changes in muscle and brain". *Phil. Trans. R. Soc. Lond. B*, 352, pp. 727-735 (1997)
- [36] Sable, Low, Whalen, Maclin, Fabiani, and Gratton. "Optical imaging of temporal integration in human auditory cortex" *European Journal of Neuroscience*, Vol. 25, pp. 298-306 (2007)
- [37] Brain. In *Wikipedia, the free encyclopedia*. Modified 20 Aug 2008, from <http://en.wikipedia.org/wiki/Brain>
- [38] Franceschini and Boas. "Noninvasive measurement of neuronal activity with near-infrared optical imaging". *NeuroImage*, 21, pp. 372- 386 (2004)
- [39] Choi, Gratton, E., Gupta, Michalos, Paunescu, Safonova, Wolf, M. and Wolf, U. "Functional Frequency-Domain Near Infrared Spectroscopy Detects Fast Neuronal Signal in the Motor Cortex". *NeuroImage* 17, pp. 1868-1875 (2002)
- [40] Talairach. In *Wikipedia, the free encyclopedia*. Modified 10 July 2008, from <http://en.wikipedia.org/wiki/Talairach>

- [41] Amita, Ishikawa, Kohno, Miyai, Oda, Seiyama, Shimizu and Tsuneishi. "Removal of the Skin Blood Flow Artifact in Functional Near-Infrared Spectroscopic Imaging Data through Independent Component Analysis". *J. of Biomedical Optics*, 12(6) 062111 (Nov/Dec 2007)
- [42] Blankertz, Curio, Dornhege, Krauledat, Losch and Müller. "Combined Optimization of Spatial and Temporal Filters for Improving Brain-Computer Interfacing". *IEEE Transactions on Biomedical Engineering*, Vol. XX, No. Y, pp. 1-8 (2006)
- [43] Blankertz, Tomioka, Lemm, Kawanabe and Müller. "Optimizing Spatial Filters for Robust EEG Single-Trial Analysis". *IEEE Signal Processing Magazine*, Vol. XX, pp. 1-12 (2008)
- [44] Hammon and de Sa. "Preprocessing and Meta-Classification for Brain-Computer Interfaces". *IEEE Trans. On Biomedical Engineering*, Vol. 54, No. 3, pp. 518-525 (2007)
- [45] Rykhlevskaia, Fabiani, and Gratton. "Lagged covariance structure models for studying functional connectivity in the brain". *NeuroImage*, 30, pp. 1203-1218 (2006)
- [46] Gratton and Fabiani. "The event-related optical signal (EROS) in visual cortex: Replicability, consistency, localization, and resolution". *Psychophysiology*, 40, pp. 561-71 (2003)
- [47] Choi, Gratton, E., Gupta, Michalos, Paunescu, Safonova, Wolf, M. and Wolf, U.. "Functional Frequency-Domain Near-Infrared Spectroscopy Detects Fast Neuronal Signal in the Motor Cortex". *NeuroImage* 17, pp. 1868-1875 (2002)
- [48] Zhan, Ledgeway, and Baker Jr. "Contrast response in visual cortex: Quantitative assessment with intrinsic optical signal imaging and neural firing". *NeuroImage* 26 pp. 330-346 (2005)
- [49] Gratton, Fabiani and Maclin. "Optimum Filtering for EROS Measurements". *Psychophysiology* 40, pp. 542-547 (2003)
- [50] Plichta, Herrmann, Baehne, Ehlis, Richter, Pauli, and Fallgatter. "Event-related functional near-infrared spectroscopy (fNIRS): Are the measurements reliable?". *NeuroImage*, 31, pp.116-124 (2006)
- [51] Matthews, Pearlmutter, Ward, Soraghan, Markham. "Hemodynamics for Brain-Computer Interfaces". *Signal Processing Magazine, IEEE*. 25(1), pp. 87-94 (2008)
- [52] Coyle, Markham and Ward. "Physiological Noise in Near-infrared Spectroscopy: Implications for Optical Brain". *IEMBS '04, 26th Annual International Conference of the IEEE*, Vol. 2, pp. 4540- 4543 (2004)
- [53] Gratton and Corballis. "Removing the Heart from the Brain: Compensation for the Pulse Artifact in the Photon Migration Signal". *Psychophysiology* 32, pp. 292-99 (1995)
- [54] Brown, Strangman and Zhang. "Adaptive filtering for global interference cancellation and real-time recovery of evoked brain activity: a Monte Carlo simulation study". *J. of Biomedical Optics* 12(4), 044014 (July/Aug 2007)
- [55] Chance, Izzetoglu, Nioka and Onaral. "Single Trial Hemodynamic Response Estimation in Block Anagram Solution Study Using fNIR Spectroscopy".....*IEEE Int. Conf. on Acoustics, Speech and Signal Processing*. Vol. 5, pp v-633-v-636 (2005)
- [56] McCluskey, Sable, Foust, Gratton, and. Rector. "Recording invertebrate nerve activation with modulated light changes". *Applied Optics*, Vol. 46, No. 10, April 1, 2007
- [57] Morren, Wolf, U., Lemmerling, Wolf, M., Choi , Gratton , De Lathauwer and Van Huffel. "Detection of fast neuronal signals in the motor cortex from functional near infrared spectroscopy measurements using independent component analysis". *Med. Biol. Eng. Computation*, vol. 42, pp. 92-99 (2004)
- [58] Cheong, Prah and Welch. "A Review of the Optical Properties of Biological Tissues". *IEEE Journal of Quantum Electronics*, Vol. 26, No. 12, pp. 2166-2185, (Dec 1990)

- [59] Yaroslavsky, Schulze, Yaroslavsky, Schober, Ulrich and Schwarzmaier. "Optical properties of selected native and coagulated human brain tissues *in vitro* in the visible and near infrared spectral range". *Phys. Med. Biol.* 47, pp. 2059–2073 (2002)
- [60] Pickering, Prahl, van Wieringen, Beek, Sterenborg, and Gemert. "Double-integrating-sphere system for measuring the optical properties of tissue". *Applied Optics*, Vol. 32, No. 4, pp. 399-410 (Feb. 1993)
- [61] Lu, Luo, Zeng and Zhu. "Effect of light losses of sample between two integrating spheres on optical properties estimation". *J. Biomedical Optics* 12(6), 064004 (Nov/Dec 2007)
- [62] Radiative Transfer Equation. In *Wikipedia, the free encyclopedia*. Modified 10 June 2008, from http://en.wikipedia.org/wiki/Radiative_transfer_equation
- [63] Firbank, Okada, and T. Delpy. "A Theoretical Study of the Signal Contribution of Regions of the Adult Head to Near-Infrared Spectroscopy Studies of Visual Evoked Responses". *NeuroImage* 8, pp. 69-78 (1998)
- [64] Gratton, Toronov, Webb, Wolf, M. and Wolf, U.. "Measurement of Brain Activity by Near-Infrared Light". *J. of Biomedical Optics* 10(1), 011008 (Jan/Feb 2005)
- [65] Okada. "The Effect of Superficial Tissue of the Head on Spatial Sensitivity Profiles for Near Infrared Spectroscopy and Imaging". *Optical Review* Vol. 7, No. 5, pp. 375-382 (2000)
- [66] Obrig, Wenzel, Kohl, Horst, Wobst, Steinbrink, Thomas and Villringer. "Near-infrared spectroscopy: does it function in functional activation studies of the adult brain?". *International Journal of Psychophysiology* 35, pp.125-42 (2000)
- [67] Steinbrink, Kempf, Villringer, and Obrig. "The fast optical signal—Robust or elusive when non-invasively measured in the human adult?". *NeuroImage* 26, pp. 996-1008 (2005)
- [68] Ogoshi and Okada. "Analysis of Light Propagation in a Realistic Head Model by a Hybrid Method for Optical Brain Function Measurement". *Optical Review* Vol 12, No. 3 pp. 264-269 (2005)
- [69] Ono, Kashio, Schweiger, Dehghanim, Arridge, Firbank and Okada. "Topographic Distribution of Photon Measurement Density Functions on the Brain Surface by Hybrid Radiosity-Diffusion Method". *Optical Review*, Vol. 7 No. 5, pp. 426-431 (2000)
- [70] Okada, Firbank, Schweiger, Arridge, Cope and Delpy. "Theoretical and experimental investigation of near-infrared light propagation in a model of the adult head". *Applied Optics*, Vol. 36, No. 1, pp. 21-31 (Jan. 1997)
- [71] Piao and Pogue. "Rapid near-infrared diffuse tomography for hemodynamic imaging using a low-coherence wideband light source". *J. Biomed. Optics* 12(1), 014016 (Jan/Feb 2007)
- [72] Haensse, Szabo, Brown, Fauchère, Niederer, Bucher, and Wolf. "New multichannel near infrared spectrophotometry system for functional studies of the brain in adults and neonates". *Optics Express* Vol. 13, No. 12, pp. 4525-4528 (June 2005)
- [73] Hoshi, Iguchi, Sato and Shimada. "Reevaluation of Near-Infrared Light Propagation in the Adult Human Head: Implications for Functional Near-Infrared Spectroscopy". *Journal of Biomedical Optics* 10(6), 064032 (November/December 2005)
- [74] Gratton and Fabiani. "The Event-Related Optical Signal: A New Tool for Studying Brain Function". *International Journal of Psychophysiology*. 42, pp. 109-121 (2001)
- [75] Chance, Li, Liu and Yang. "Low-cost frequency-domain photon migration instrument for tissue spectroscopy, oximetry, and imaging". *Optical Engineering*, 36(5), pp. 1562-1569 (May 1997)
- [76] Gratton and Fabiani. "In Vivo Optical Imaging of Brain Function". In R. Parasuraman and M. Rizzo (Eds.) *Neuroergonomics: The Brain at Work*, pp. 65-81. CRC Press 2002.
- [77] Gratton, Fabiani, Low and Maclin. "Signal-to-Noise Ratio of Event-Related Optical Signals". *IEEE Engineering in Medicine and Biology Magazine*, pp. 46-52 (July/Aug 2007)
- [78] Dell, Fabiani, Garnsey, Gratton, Lee, Sullivan and Tse. "Imaging Cortical Dynamics of Language

- Processing with the Event-Related Optical Signal”. *Proceedings of the National Academy of Sciences*, Vol. 104, no. 43, pp. 17157-17162, Oct. 23, 2007
- [79] Wubbels et al. “Exploring Calibration Techniques for Functional Near-Infrared Imaging (fNIR) Controlled Brain-Computer Interfaces”. *Augmented Cognition*, HCII 2007, LNAI4565, pp. 23–29, Springer-Verlag Berlin Heidelberg (2007)
- [80] Ranganathaa, Hoshi, Guana. “Near Infrared Spectroscopy based Brain-Computer Interface”. *Third Intl. Conf. on Experimental Mechanics and Third Conf. of the Asian Committee on Experimental Mechanics*, edited by Quan, Chau, Asundi, Wong, and Lim, Proc. of SPIE Vol. 5852 (SPIE, Bellingham, WA, 2005)
- [81] Kacprzak, Liebert, Sawosz, Z`olek and Maniewski. “Time-Resolved Optical Imager for Assessment of Cerebral Oxygenation”. *Journal of Biomedical Optics* 12(3), 034019 (May/June 2005)
- [82] Gratton, G., Low, K. A., Maclin, E. L., Brumback, C. R., Gordon, B. A., & M. Fabiani . “Time course of activation of human occipital cortex measured with the event-related optical signal (EROS)”. *Biomedical Optics 2006 Technical Digest* (Optical Society of America, Washington, DC, 2006), MD4
- [83] Harper, Kristensen, Poe and Rector. “Light Scattering Changes Follow Evoked potentials From Hippocampal Schaeffer Collateral Stimulation”. *J. Neurophysiology* Vol. 78, pp. 1707-1713, 1997
- [84] Hillman. “Optical Brain Imaging In Vivo: Techniques and Applications from Animal to Man”. *Journal of Biomedical Optics* 12(5), 051402 (September/October 2007)
- [85] Matti Kinnunen and Risto Myllylä. “Application of optical coherence tomography, pulsed photoacoustic technique, and time-of-flight technique to detect changes in the scattering properties of a tissue-simulating phantom”. *Journal of Biomedical Optics* 13(2), 024005 (March/April 2008)
- [86] Lieke et al. “Optical Imaging of Cortical Activity: real-time imaging using extrinsic dye-signals and high resolution imaging based on slow intrinsic-signals”. *Annu. Rev. Physiol.*, Vol. 51, pp. 543-59, 1989
- [87] Boppart, Oldenburg, Xu and Marks. “Optical probes and techniques for molecular contrast enhancement in coherence imaging”. *Journal of Biomedical Optics* 10(4), 041208 (July/August 2005)
- [88] Yaqoob, Psaltic, Feld and Yang. “Optical phase conjugation for turbidity suppression in biological samples”. *Nature Photonics*, Volume 2, pp. 100-115 (Feb 2008)
- [89] Wolpaw (Guest Editor) et al. “Brain–Computer Interface Technology: A Review of the First International Meeting”. *IEEE Transaction on Rehabilitation Engineering*, Vol. 8, No. 2, pp. 164-173 (June 2000)
- [90] Tomas E. Ward, Christopher J. Soraghan, Fiachra Matthews, and Charles Markham. “A Concept for Extending the Applicability of Constraint-Induced Movement Therapy through Motor Cortex Activity Feedback Using a Neural Prosthesis”. *Comput. Intell Neurosci.* (2007)
- [91] Sanchez and Principe. “Optimal Signal Processing for Brain-Machine Interfaces”. In *Handbook of Neural Engineering*, Edited by Metin Akay
- [92] Mason, Bashashai, Fatourehchi, Navarro and Birch. “A Comprehensive Survey of Brain Interface Technology Designs”. *Annals of Biomedical Engineering*, Vol. 35, No. 2, pp. 137–169, (Feb 2007)
- [93] Benjamin Blankertz, Ryota Tomioka, Steven Lemm, Motoaki Kawanabe, Klaus-Robert Müller . “Optimizing Spatial Filters for Robust EEG Single-Trial Analysis”. *IEEE Signal Processing Magazine*, Vol. XX (2008)
- [94] Blankertz et al. “The BCI Competition III: Validating Alternative Approaches to Actual BCI Problems”. *IEEE Transactions on Neural Systems and Rehabilitation Engineering*, Vol. 14, No. 2, (June 2006)
- [95] M Fatourehchi, R K Ward and G E Birch. “A self-paced brain–computer interface system with a low false positive rate”. *J. Neural Eng.* 5, pp. 9–23 (2008)

- [96] Utsugi, Obata, Sato, Katsura, Sagara, Maki and Koizumi. "Development of an Optical Brain-machine Interface". *Proceedings of the 29th Annual International Conference of the IEEE EMBS.*, August 23-26, 2007
- [97] Elena Rykhlevskaia, Monica Fabiani, and Gabriele Gratton. "Lagged covariance structure models for studying functional connectivity in the brain". *NeuroImage* 30, pp. 1203-1218 (2006)
- [98] Shirley M Coyle, Tomás E Ward and Charles M Markham. "Brain-computer interface using a simplified functional near-infrared spectroscopy system". *J. Neural Engineering* 4, pp. 219-26 (2007)
- [99] Coyle, Ward, Markham and McDarby. "On the suitability of near-infrared (NIR) systems for next-generation brain-computer interfaces". *Physiological Measurement*, 25, pp. 815-822 (2004)
- [100] Nithya Sambasivan and Melody Moore Jackson. "Designing Pervasive Brain-Computer Interfaces". In A. Holzinger (Ed.): *USAB 2007, LNCS 4799*, pp. 267-272, Springer-Verlag Berlin Heidelberg 2007
- [101] Birbaumer and Cohen. "Brain-computer interfaces: communication and restoration of movement in paralysis". *J. Physiol.* 579.3, pp. 621-636 (2007)
- [102] Birbaumer. "Breaking the silence: Brain-computer interfaces (BCI) for communication and motor control". *Psychophysiology* 43, pp. 517-532 (2006)
- [103] Klaus-Robert Müller, Michael Tangermann, Guido Dornhege, Matthias Krauledat, Gabriel Curio, Benjamin Blankertz. "Machine learning for real-time single-trial EEG-analysis: From brain-computer interfacing to mental state monitoring". *Journal of Neuroscience Methods* 167, pp. 82-90 (2008)
- [104] S-S. Yoo, T. Fairney, N-K. Chen, L. P. Panych, H-W. Park, S-Y. Lee, F. A. Jolesz. "Brain-Computer-Interface using fMRI: Spatial Navigation by Thoughts". *Proceedings of the Intl. Society of Mag. Reson. Med* 11, pp. 733 (2004)
- [105] Weiskopf et al. "Principles of a brain-computer interface (BCI) based on real-time functional magnetic resonance imaging (fMRI)". *IEEE Transactions on Biomedical Engineering*, Vol. 51, No. 6, pp. 966-970 (June 2004)
- [106] George and Yao. "Near-infrared imaging of fast intrinsic optical responses in visible light-activated amphibian retina". *Journal of Biomedical Optics* 11(6), 064030 (Nov/Dec 2006)